Cryogenics 132 (2023) 103685

Contents lists available at ScienceDirect

Cryogenics

journal homepage: www.elsevier.com/locate/cryogenics

Intermediate cooling from pulse tube refrigerator regenerators operating in the real-fluid regime

Ryan Snodgrass [a,b,*], Gregory Swift [c], Joel Ullom [a,b], Scott Backhaus [a,b]

[a] National Institute of Standards and Technology, Boulder, CO 80305, United States of America
[b] Department of Physics, University of Colorado Boulder, Boulder, CO 80309, United States of America
[c] Swift Science and Engineering, Santa Fe, NM 87506, United States of America

A B S T R A C T

Under some circumstances, pulse tube refrigerator regenerators operating in the real-fluid regime can absorb a large amount of heat between their warm and cold ends without a decrease to cooling power at their cold heat exchanger. Experiments and analysis show that this extra source of cooling is available because real-fluid thermodynamics modify the temperature profile to direct this additional heat flow toward the warm rather than the cold heat exchanger. Intermediate cooling capacity measurements in a two-stage, dual-inlet pulse tube refrigerator show that the cooling available is larger than commonly appreciated, 2 W at 7.5 K for the particular cryocooler investigated—almost nine times the 0.23 W available at the 3 K cold end. An analytical model is developed that predicts the dependence of injection temperature versus amount of injected heat and location along the regenerator; results from the model agree well with those from experiment and those generated using common numerical codes. This model is also used to explore strategies to increase the available intermediate cooling. For very high amounts of regenerator cooling, the shape of the temperature profile fundamentally changes and power flow changes occur at the cold—rather than warm—heat exchanger. Our results can guide users on how to best utilize this source of cooling and inspire designers to plan for large amounts of intermediate cooling.

1. Introduction

The second-stage regenerator of a two-stage, low-frequency pulse tube refrigerator (PTR) can absorb heat along its length with little to no effect on the cooling available at the cold heat exchanger.[1] We call this heat absorption *intermediate* cooling since it takes place at a temperature between that of the warm and cold ends. The cooling available from the regenerator can be very large: for example, the intermediate cooling at 7-8 K can be an order of magnitude higher than the cooling from the cold heat exchanger at 3 K. This effect is often used for cooling returning ^{3}He in dilution refrigerators [1] and for cooling conductive loads such as coaxial cables running to a low-temperature experiment. Cooling of cryogenic sorption pumps is another possible application. The use of intermediate cooling leaves more refrigeration available at the cold heat exchanger and may allow smaller, lower-power cryocoolers to accomplish the same function as their larger counterparts.

Although intermediate cooling is often used in commercial cryostats, a comprehensive understanding of the effect is still lacking. Early studies [2,3] identified loss mechanisms in the regenerator as the source of intermediate cooling capacity. Later studies [4–6] reported a limited set of experimental observations of intermediate cooling but did not explain the mechanisms or limits of the effect. Real-fluid effects are known to dominate the power flow in these regenerators and cause the temperature profile to be flat at the cold end [7,8]; however, no publication has thoroughly explained the connection between real-fluid effects and intermediate cooling.

Recently, we used intermediate heat injection to investigate powers in low-temperature regenerators operating in the real-fluid regime [9]; the methods presented in that study allow—for example—the estimation of acoustic power and steady mass flow through these regenerators. We have also studied the available intermediate cooling in Gifford-McMahon cryocoolers [10], and how to optimally absorb common heat loads using PTR regenerators [11]. In another study, we showed that azimuthal regenerator temperature asymmetries are present and likely caused by real-fluid effects [12]. Taken together, our previous works demonstrate that a deeper understanding of cryocooler physics can be gained by analyzing the response of the regenerator temperature profile to intermediate heat injection, which is the approach we take in this study.

While this work focuses on low-frequency, Gifford-McMahon type cryocoolers, the real-fluid and finite-heat-capacity effects described are equally important in high-frequency cryocoolers operating at very low

* Corresponding author at: National Institute of Standards and Technology, Boulder, CO 80305, United States of America.
E-mail address: ryan.snodgrass@nist.gov (R. Snodgrass).

[1] However, the cooling available at the first-stage heat exchanger decreases, as shown in Section 3.2.

https://doi.org/10.1016/j.cryogenics.2023.103685
Received 23 January 2023; Received in revised form 17 April 2023; Accepted 18 April 2023
Available online 20 April 2023
0011-2275/Published by Elsevier Ltd.

Nomenclature

Powers	
$\dot{E}_2$	Acoustic or pV power
$\dot{H}_2$	Total power
$\dot{H}_\beta$	Pressure dependence of enthalpy (real-fluid) power
$\dot{H}_\epsilon$	Finite heat capacity power
$\dot{H}_\kappa$	Thermal conductivity power
$\dot{H}_m$	Steady mass flow power
$\dot{H}_{\nabla T}$	Flow across temperature gradient power
$\dot{Q}$	Cooling power
Solid and fluid properties	
β	Thermal expansion coefficient
ϵ	Volumetric specific heat ratio
μ	Dynamic viscosity
ρ	Density
σ	Prandtl number
c_p	Specific heat at constant pressure
h	Enthalpy per unit mass
k	Thermal conductivity
m	Molar mass
T	Temperature
Regenerator properties	
ϕ	Porosity
A_g	Fluid cross sectional area
L	Total length
r_h	Hydraulic radius
x	Axial location starting at the warm end
Subscripts	
0	In the base state; at $x = 0$
κ	Thermal conductivity related
ν	Viscosity related
c	Cold; at the cold end
h	At high pressure
i	Imaginary part
int	Intermediate, i.e. between warm and cold
l	At low pressure
m	Cycle mean
min	Minimum; at the minimum temperature
r	Real part
s	Solid
w	Warm; at the warm end
Thermoacoustic properties	
δ	Penetration depth
$\dot{N}$	Steady molar flow rate
ω	Frequency of thermoacoustic oscillations
f	Spatially averaged thermoacoustic function
p	Pressure
U	Volume flow rate

temperatures, such as in [13]. Therefore, the power analysis presented here should be broadly useful.

In the following, we use a thermoacoustic framework to explain how real-fluid effects dominate power in low-temperature regenerators and how this leads to the capacity for intermediate cooling. Experiments using intermediate heat injection for a two-stage PTR are described. Analysis of the total power in the regenerator is used to explain the changes to the temperature profile that occur when intermediate heat is applied. This analysis leads to a model that predicts the temperature of intermediate heat injection, and the predictions of the model are compared to measurements and to results from the numerical codes REGEN and DeltaEC.[2] We then explore the behavior of the regenerator for very high amounts of intermediate heat injection; interestingly, for very high heats the end of the regenerator with fixed power reverses. We conclude by using the model as a guideline to recommended strategies for increasing the amount of intermediate cooling available.

1.1. Enthalpy in the real-fluid regime

The second-stage regenerators of low-frequency (~1 Hz) PTRs commonly span temperatures between about 50 K and 4 K, and have a helium fill pressure of about 1 MPa. Under these conditions, helium does not behave like an ideal gas. Enthalpy changes dh in the fluid no longer depend only upon temperature changes dT, but also depend on changes in pressure dp:

$$dh = c_p dT + \frac{(1 - T\beta)}{\rho} dp, \tag{1}$$

where c_p, ρ, and β are the fluid's specific heat at constant pressure, density, and thermal expansion coefficient (equal to $1/T$ for an ideal gas). Near 3 K or 4 K, the pressure-driven component of enthalpy results in a power that is almost as large as the acoustic or pV power. As we will show in the following sections, this power is fundamental in determining the cooling power of 4 K cryocoolers.

1.2. Total power

A regenerator transmits time-dependent pressure and flow while simultaneously isolating the cold heat exchanger from the warm heat exchanger by minimizing the total power $\dot{H}_2$ flowing along its length. When directed toward the cold heat exchanger, $\dot{H}_2$ directly subtracts from its cooling power. To compute $\dot{H}_2$, we use the thermoacoustic framework developed by Rott [14] and Swift [15] that accounts for real-fluid effects and finite heat capacity of the regenerator materials. A simplified expression of the one-dimensional, thermoacoustic total power is derived in Appendix A. The derivation starts with the general form of the total power equation and expands it in the limit of small hydraulic radius r_h compared to thermal penetration depth[3] δ_κ (r_h/δ_κ is of order 0.1 for 1 Hz, 4 K regenerators). The derivation also approximates porous-media regenerators as parallel plate regenerators, making the mathematics much more tractable but retaining the important physical effects. The resulting expression from Appendix A is

$$\dot{H}_2(x) \approx (1 - T_m\beta)\dot{E}_2 + \left(\frac{\epsilon_r}{1+\epsilon_r}\right) T_m\beta\dot{E}_2 + \dot{N}mh - \frac{\rho_m c_p |U_1|^2}{2\omega A_g}\left[\frac{\epsilon_i}{(1+\epsilon_r)^2} + \frac{r_h{}^2/\delta_\kappa{}^2}{(1+\epsilon_r)}\right]\frac{dT_m}{dx} - (A_g k + A_s k_s)\frac{dT_m}{dx}, \tag{2}$$

where x is the distance along the regenerator axis and the warm end is taken as $x = 0$; by this convention dT_m/dx is negative and the two dT_m/dx power terms in Eq. (2) are positive. The acoustic or pV power is $\dot{E}_2$, $\dot{N}$ is the steady molar flow rate, m is the molar mass, and h is the enthalpy per unit mass. Subscript m represents the cycle mean, so T_m

[2] Results from these codes may be found in Supplementary 1.

[3] Defined in Eq. (A.2).

and ρ_m are the mean temperature and density of the fluid. The angular frequency of the thermoacoustic oscillations is ω and U_1 is the oscillating volume flow rate (a phasor). The cross-sectional area and thermal conductivity of the fluid are A_g and k, respectively. The ratio of the fluid to solid volumetric heat capacities is $\epsilon_r = \phi\rho_m c_p/(1-\phi)\rho_s c_s$, where ϕ is the porosity, and k_s, ρ_s, and c_s are the thermal conductivity, density, and specific heat of the solid, respectively. The ratio of volumetric heat capacities also has an imaginary component ϵ_i that is discussed in Appendix A.

The total power is written in shorthand as

$$\dot{H}_2 \approx \dot{H}_\beta + \dot{H}_\epsilon + \dot{H}_m + \dot{H}_{\nabla T} + \dot{H}_\kappa, \qquad (3)$$

where the order of terms on the right hand side of Eq. (3) corresponds to that on the right hand side of Eq. (2). Each term represents a different mode of power transport in the regenerator. Critical to studying $\dot{H}_2$ is an understanding that if heat is exchanged with external sources or sinks only at the regenerator ends, total power is the same at every location and $d\dot{H}_2/dx = 0$. As T_m changes from the warm end temperature T_w to the cold end temperature T_c, total power remains constant, but it shifts among the five terms in Eqs. (2) and (3). We will now proceed to discuss each.

The $\dot{H}_{\nabla T}$ and $\dot{H}_\kappa$ terms only carry power when $dT_m/dx \neq 0$. The thermal conduction mode $\dot{H}_\kappa$ is typically negligible and will not be considered further in this work. The $\dot{H}_{\nabla T}$ term is due to the helium oscillating with $|U_1|$ along the temperature gradient with imperfect thermal contact (see the $(r_h/\delta_\kappa)^2$ factor in Eq. (2)) generating local temperature and enthalpy oscillations. These enthalpy oscillations are convected by another factor of $|U_1|$ resulting in time-averaged power. Under common operating conditions of 4 K regenerators, $\dot{H}_{\nabla T}$ is significant at the warm end but negligible at the cold end. The form of $\dot{H}_{\nabla T}$ in Eq. (2) arises from the parallel plate approximation discussed in Appendix A, which has no Reynolds number dependence of the heat transfer coefficient.

The $\dot{H}_\beta$ and $\dot{H}_\epsilon$ terms in Eqs. (2) and (3) strongly depend on T_m but are independent of dT_m/dx. They are both proportional to $\dot{E}_2 = \mathrm{Re}[p_1\tilde{U}_1]/2$ and transport power when $\dot{E}_2$ is nonzero.[4] Acoustic power is determined by p_1 and U_1, which are the pressure and volumetric flow rate phasors, respectively, and the tilde above U_1 denotes the complex conjugate. Our method for estimating acoustic power at the cold end of the regenerator is given in Appendix B, which is the basis for $\dot{E}_2(T_m)$ used for much of the analysis in this manuscript. In the ideal gas regime it is common to estimate that acoustic power scales simply by the ratio of the temperatures; however, in the real-fluid regime the thermal expansion coefficient is fundamental in determining the scaling of $\dot{E}_2$. Insufficient solid heat capacity can also affect the scaling of acoustic power. See Appendix C for details on how to estimate $\dot{E}_2$ at any temperature between T_w and T_c.

Both $\dot{H}_\beta$ and $\dot{H}_\epsilon$ are due to oscillating pressure, but in different ways. For $\dot{H}_\beta$, p_1 in a real fluid directly creates an oscillating enthalpy via the $(1-T_m\beta)$ term in Eq. (1). This mode of power is due entirely to real-fluid properties that are significant below about 30 K (Fig. 1a).

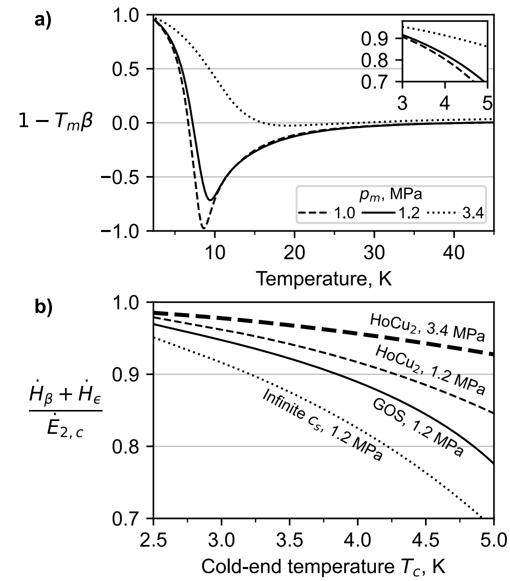

Fig. 1. a) $1-T_m\beta$ vs temperature for helium at three mean pressures, showing that this quantity can be either positive or negative and varies widely in the real-fluid regime, i.e. less than about 30 K at these pressures. b) The power contribution from real-fluid effects and finite-heat-capacity effects normalized by acoustic power at the cold end, calculated for two materials commonly used at the cold end of low-temperature regenerators. GOS is the common name for Gd_2O_2S. A fictitious material with infinite solid heat capacity ($\epsilon_r = 0$) represents the contribution from real-fluid effects alone. If thermal buffer tube losses are negligible, then the gross cooling power available at T_c is one minus the plotted number multiplied by $\dot{E}_{2,c}$. For example, a GOS regenerator at 1.2 MPa and T_c = 3.8 K gives about 10% of the cold-end acoustic power as the cooling power. See Section 3.1 for more details.

This mode of power cannot be mitigated by the regenerator. For $\dot{H}_\epsilon$, the finite heat capacity of the regenerator solid cannot absorb all of the heat of compression, resulting in a local temperature and enthalpy oscillation in the fluid. For a mean pressure of 1.2 MPa, the heat capacity of helium is maximum at 9 K, so near this temperature these enthalpy oscillations can be very large [17]. The real-fluid and finite-heat-capacity enthalpy oscillations are convected by U_1, resulting in $\dot{H}_\beta$ and $\dot{H}_\epsilon$, respectively.

The power carried by any steady mass flow through the regenerator (i.e., streaming) is $\dot{H}_m$. The PTR used in this work is a dual-inlet pulse tube refrigerator (DIPTR) [18], a common topology for low-frequency PTRs. DIPTRs have a torodial flow path around the regenerators allowing Gedeon streaming [19] which carries $\dot{H}_m$ through the regenerators. In [9] we developed a method (Appendix B) to estimate the steady molar flow rate $\dot{N}$ and found it to be near 1 mmol/s. Since that time, we have improved our understanding of acoustic power scaling (Appendix C) and now estimate $\dot{N}$ to be closer to 5 mmol/s in the second stage regenerator of this particular pulse tube.

1.3. Impact of real-fluid effects and finite regenerator heat capacity

The real-fluid power $\dot{H}_\beta$ cannot be mitigated, even in high-performance regenerators. Below about 7 K, $(1-T_m\beta)$ grows rapidly (Fig. 1a) and $\dot{H}_\beta$ often becomes dominant over the other power modes. Since $\dot{H}_\beta$ depends on T_m but not dT_m/dx and total power must be constant at any regenerator location x (in the absence of intermediate heat), the temperature profile near the cold end of regenerators operating below about 7 K is typically very flat [9,12,20,21]. Finite-heat-capacity effects also contribute to a flattening of the temperature profile, since $\dot{H}_\epsilon$ too depends on T_m and not dT_m/dx.

The terms $\dot{H}_\beta$, $\dot{H}_\epsilon$, and $\dot{H}_m$ determine the total power at the cold end $\dot{H}_{2,c}$ when the temperature gradient there is very small. For convenience, we adapt the convention $h(T_c) = 0$, so $\dot{H}_{2,c} = \dot{H}_{\beta,c} + \dot{H}_{\epsilon,c}$. When

[4] The subscript in $\dot{E}_2$ indicates that acoustic power is a product of two first-order acoustic variables. Although the thermoacoustic framework was developed for sinusoidal thermodynamics, low-frequency PTRs are of the valved ("GM") type, so the pressure and flow rate phasors can be shaped more like square waves. Swift argued that harmonic analysis should still be relatively accurate for power analyses because the additional power terms to consider are fourth-order or higher [15]. Products containing odd-order terms such as $\sin(\omega t)\sin(2\omega t)$ time average to zero, so there is no power term of third-order to consider. If the amplitude of the pressure oscillation in a valved PTR is about half of the mean pressure, then thermoacoustic analysis at the fundamental frequency is expected to give results for power with errors about $(0.5)^2 = 25\%$. Pressure measurements in the regenerators of these valved type coolers show that the phasors might be more sinusoidal than expected [16], so errors may be smaller than 25%.

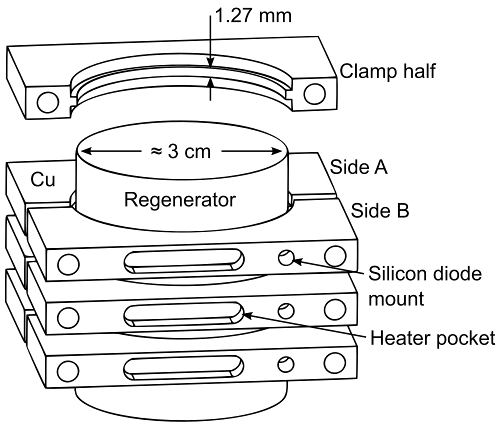

Fig. 2. Detail of the thermometer and heater mounting in the experimental setup. Twenty-one full clamp assemblies were fastened to the second-stage regenerator as shown; 10 were used for temperature measurement and 10 for heat input (in an alternating fashion).

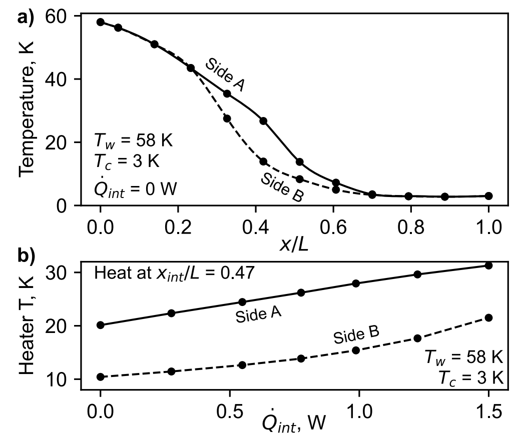

Fig. 3. a) An example of the two regenerator temperature profiles (one for each side) with no intermediate heat applied. Lines are cubic-spline fits. b) The cubic-spline fits were also used to evaluate the temperature of heat injection on each side when heat was applied to the regenerator at x_{int}.

heat is exchanged only at the regenerator ends, $d\dot{H}_2/dx = 0$, and total power at the cold end sets the power for the entire regenerator.

This total power depends only on acoustic power $\dot{E}_{2,c}$ and fluid and regenerator material properties at T_c (through β and ϵ_r). Fig. 1b plots $(\dot{H}_\beta + \dot{H}_\epsilon)/\dot{E}_{2,c}$, showing that $\dot{H}_2$ approaches $\dot{E}_{2,c}$ as the minimum temperature in the regenerator approaches 2 K or 3 K. As will be determined in Section 3.1, the cold-end cooling power is $\dot{Q}_c = \dot{E}_{2,c} - (\dot{H}_\beta + \dot{H}_\epsilon)$, showing that real-fluid effects and finite heat capacity are responsible for the small amount of cooling power available at the cold heat exchanger. Furthermore, Fig. 1b shows that $\dot{H}_\beta$ dominates total power around 2 K or 3 K, so real-fluid effects are primarily responsible for limiting cooling power. Finite solid heat capacity reduces the cooling power by approximately a factor of two past the limit set by real-fluid effects. The cryocoolers of interest in this study typically operate at mean pressures near 1 MPa, but Fig. 1a also shows that at higher mean pressures the real-fluid effects consume a much larger fraction of the available cooling power. At 4 K and 1 MPa, $1 - T_m\beta$ is 0.80, while at 3.4 MPa it is 0.91—an extra $0.11\dot{E}_{2,c}$ of cooling power is lost to real-fluid effects (the pressure dependence of enthalpy).

2. Methods

2.1. Equipment and instrumentation

Our experimental platform is a commercial, low-frequency (1.4 Hz) DIPTR. Its second-stage regenerator is encased in a thin-wall, stainless-steel tube, and the solid matrix is divided into three subsections where each subsection is a sphere bed of a different material. We instrumented this regenerator with thermometers and heaters using a series of opposing copper clamps (Fig. 2). Each pair of clamps makes thermal contact with the stainless steel tube around its circumference for nearly 360° but over a thickness of just 1.27 mm to minimize its effect on the temperature profile.[5] Clamp-halves are bolted together using 4-40 UNC stainless-steel screws, and a thin layer of thermal grease was applied to the lip of the clamps before being fixed to the regenerator. Twenty-one pairs of evenly-spaced clamps were fastened to the regenerator—10 pairs for temperature measurement, and 10 pairs for heat injection (one pair was unused). This provides a spatial resolution of about 1.5 cm for both temperature measurement and heat injection.

Heat injection clamps have a resistance heater epoxied into the pockets shown in Fig. 2—one on each clamp half so heat was applied in an azimuthally uniform manner. Each clamp-pair can apply up to 3.375 W using a 50 Hz pulse-width modulated signal. Heat can be applied simultaneously at any combination of clamps. All heaters have output resolution near 0.1 mW.

Temperatures were measured using seventeen silicon diode thermometers. The diodes were calibrated to an accuracy of ± 25 mK at temperatures less than 25 K and to ± 75 mK for higher temperatures. The three clamps nearest to the warm end have a single thermometer while the seven clamps nearest to the cold end have thermometers on both clamp-halves. The clamp-halves are thermally isolated from each other by the relatively long stainless steel screws, which enabled crude measurement of azimuthal temperature variation. Thermometers were also placed on the warm and cold heat exchangers of the second-stage regenerator. These heat exchangers were temperature regulated with a typical accuracy of ± 20 mK using a temperature controller. The cold end temperature T_c was regulated to 3 K for most experiments (to higher temperatures in Section 5), while the temperature at the warm end T_w was adjusted to fixed values between 42 K and 58 K.

Unless otherwise specified, all data shown in this manuscript were recorded at steady state. Experiments consisted of changing the heat applied to an intermediate heater, and then allowing the temperature profile to reach steady state—when all 19 thermometers changed by less than 32 mK over one minute. Oscillations in temperature driven by the oscillating pressure and flow were filtered out by commercial temperature monitors to give the mean temperature T_m at each thermometer location.

2.2. Measurement of the heat injection temperature

Fig. 3a is an example of the regenerator temperature profile without intermediate heat $\dot{Q}_{int}$ applied. Throughout this manuscript, axial locations are referenced normalized by regenerator length L, with the warm end at $x/L = 0$. Using the 17 temperature measurements along the regenerator and the two measurements on the heat exchangers, two cubic-spline curves are fit to the temperature data, one for each regenerator side. The three T_m measurements closest to the warm end are assumed to be the same for both regenerator halves, which previous work for this cryocooler [12] shows to be a good approximation. Intermediate heat $\dot{Q}_{int}$ is always applied in-between temperature measurements, and the temperature of heat injection is estimated using the cubic-spline fits at the injection location.

[5] We believe the clamps affect the behavior of the regenerator minimally; this topic is explored in Supplementary 2.

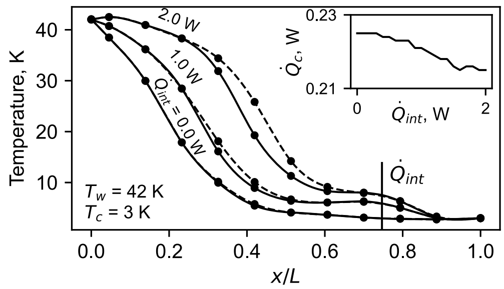

Fig. 4. The temperature profile of the regenerator with 0 W, 1 W, or 2 W of $\dot{Q}_{int}$ applied at the vertical line. Solid and dashed lines are for two opposing sides of the regenerator. Inset shows that the cooling power at the cold heat exchanger drops just 10 mW out of 225 mW when 2 W of intermediate heat was injected.

Fig. 3b shows an example of why the temperature asymmetry[6] must be considered when determining heat injection temperature. When heat was applied near the middle of the regenerator the injection temperature differed by about 10 K between the two sides. In subsequent analysis, the temperature at any location along the regenerator is approximated as the mean of the two temperature profiles.

3. Regenerator response to intermediate heat

3.1. Regenerator temperature profile and $\dot{Q}_c$

Fig. 4 shows that, in the absence of intermediate heat ($\dot{Q}_{int} = 0$), the temperature gradient in the first half of the regenerator (near the warm end) is large and negative, and $T_m(x)$ in the second half is close to T_c with a very small gradient. As $\dot{Q}_{int}$ at[7] $x_{int}/L = 0.75$ is increased, the magnitude of the temperature gradient near the warm end decreases and the temperature profile shifts towards the cold end. Although $T_m(x)$ undergoes significant change, $\dot{Q}_c$ changes by less than 5% with 2 W applied to the regenerator (Fig. 4 inset). This intermediate heat load is about an order of magnitude higher than the cooling available at 3 K.

We use this behavior to gain an understanding of how $\dot{H}_2$ and $\dot{E}_2$ depend on $\dot{Q}_{int}$. This behavior was analyzed previously [9] but is summarized here. Consider a control surface that is normal to the regenerator axis and just inside its cold-end face. If the temperature at the cold-end face is below approximately 7 K (i.e., the profile is nearly flat at the cold end), the discussion in Section 1.3 shows that the total power at this face is

$$\dot{H}_{2,c} \approx \dot{H}_{\beta,c} + \dot{H}_{\epsilon,c} = \left(1 - \frac{T_c \beta_c}{1 + \epsilon_{r,c}}\right) \dot{E}_{2,c}, \tag{4}$$

where the subscript c denotes evaluation at the cold-end temperature.[8] Since β and ϵ_r are only functions of T_m (p_m is nearly constant in these measurements), Eq. (4) shows that the power at the cold end only depends on T_c and $\dot{E}_{2,c}$.

In our experiments, T_c is fixed by a temperature controller. The acoustic power $\dot{E}_{2,c}$ at this face should also be nearly fixed because it is primarily determined by the properties of the DIPTR flow network, which is entirely at ambient temperature. Furthermore, our measurements suggest only small changes to $\dot{E}_2$. As discussed in Supplementary 3, $|p_1|$ was estimated using measurements at the inlet and outlet of the compressor. Fig. 5 shows that $|p_1|^2$ typically changes by less than 4% even for $\dot{Q}_{int}$ up to 2.5 W; $\dot{E}_2$ is expected to vary by a similar amount because $\dot{E}_2 = \mathrm{Re}[p_1 \tilde{U}_1]/2$ (see Supplementary 3 for more details). This is a relatively small change to $\dot{E}_2$ and we proceed by neglecting the dependence of $\dot{E}_2$ on $\dot{Q}_{int}$. With fixed $\dot{E}_{2,c}$ and T_c, Eq. (4) implies fixed $\dot{H}_{2,c}$.

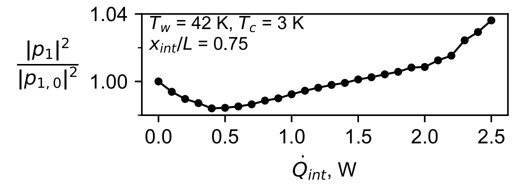

Fig. 5. The pressure amplitude squared as a function of intermediate heat, normalized by the pressure amplitude with no heat applied $|p_{1,0}|$ squared.

We confirm this conclusion by considering a First Law control volume that encloses the cold end of the regenerator and the cold heat exchanger—a pillbox with one face just inside the regenerator cold end (as above) and its second face just beyond the opposite side of the cold heat exchanger. The balance of energy flowing into this control volume shows that cooling power at the cold end is

$$\dot{Q}_c \approx \dot{E}_{2,c} - \dot{H}_{2,c} \approx \frac{T_c \beta_c}{1 + \epsilon_{r,c}} \dot{E}_{2,c}, \tag{5}$$

where we have assumed an ideal thermal buffer tube that has $\dot{H}_2 = \dot{E}_2$ (ignoring $\dot{H}_m$ because by our convention $h(T_c) = 0$). The data in Fig. 4 show that, with T_c fixed, $\dot{Q}_c$ is nearly fixed, which confirms our conclusion that $\dot{E}_{2,c}$ and $\dot{H}_{2,c}$ are fixed as $\dot{Q}_{int}$ is varied and T_c regulated.

Next, we consider a First Law control volume to analyze $\dot{Q}_{int}$—a pillbox with one face just inside the regenerator cold end (as above) and a second face between the warm end and the point where $\dot{Q}_{int}$ is injected. The balance of energy flows into this control volume shows

$$\dot{H}_{2,w} = \dot{H}_{2,c} - \dot{Q}_{int}, \tag{6}$$

where $\dot{H}_{2,w}$ is the power entering the warm-end face of the control volume. Since $\dot{Q}_{int}$ is the only heat injected along the regenerator, $\dot{H}_{2,w}$ and $\dot{H}_{2,c}$ can be interpreted as the power at all points upstream and downstream of the heat injection point, respectively. The analysis in the previous paragraph showed that $\dot{H}_{2,c}$ does not change with $\dot{Q}_{int}$, so Eq. (6) shows that $\dot{H}_{2,w}$—the power at all points between the heat injection point and the warm end—decreases by approximately $\dot{Q}_{int}$.

Equations (5) and (6) show how the regenerator powers change to accommodate $\dot{Q}_{int}$. When T_c is fixed, real-fluid effects and the insensitivity of the DIPTR flow network to changes in $T_m(x)$ fix $\dot{E}_{2,c}$, $\dot{H}_{2,c}$, and $\dot{Q}_c$. Instead of changing those variables, the regenerator accommodates $\dot{Q}_{int}$ by reducing $\dot{H}_{2,w}$. If T_w is fixed by a temperature controller and streaming does not change when $\dot{Q}_{int}$ is applied, the first three terms of Eq. (2) are fixed. The only mechanism for a reduction in $\dot{H}_{2,w}$ is a decrease in the magnitude of dT_m/dx at the warm end, which is consistent with the experimental observations in Fig. 4. Between $x = 0$ and x_{int}, changes to T_m-dependent power terms and dT_m/dx-dependent power terms must combine to satisfy $d\dot{H}_2/dx = 0$. The decrease in the magnitude of the temperature gradient at the warm end causes the region of sharp dT_m/dx to shift towards the cold end.

The analyses used to reach Eqs. (5) and (6) are no longer valid for the PTR analyzed here at T_c above about 7 K. Measurements in Fig. 6a show that, near this T_c, the temperature profile inverts so it is relatively flat near the warm end and has a significant temperature gradient at the cold end. That relatively small changes to T_c can cause such drastic changes in the shape of the overall temperature profile was predicted by de Waele [7]. For the inverted profile, total power at the cold end $\dot{H}_{2,c}$ is determined by both T_m and dT_m/dx-dependent terms from Eq. (2). As $\dot{Q}_{int}$ is increased and T_c is held fixed, $\dot{H}_{2,c}$ increases by an amount very close to $\dot{Q}_{int}$ (Fig. 6b). The increase in $\dot{H}_{2,c}$ is reflected by the decrease to $\dot{Q}_c$, as required by the intermediate step of Eq. (5) with fixed $\dot{E}_{2,c}$. Inversion of the temperature profile has also been observed at lower T_c for very high amounts of $\dot{Q}_{int}$, as discussed further in Section 5.

[6] For more details on the asymmetry see [12].

[7] This location was chosen because it is not so close to the cold end that it decreases $\dot{Q}_c$, as will be discussed in Section 3.2.

[8] More precisely, the power is determined by the minimum temperature of the regenerator, which may differ slightly from the cold-end temperature. See Appendix B.

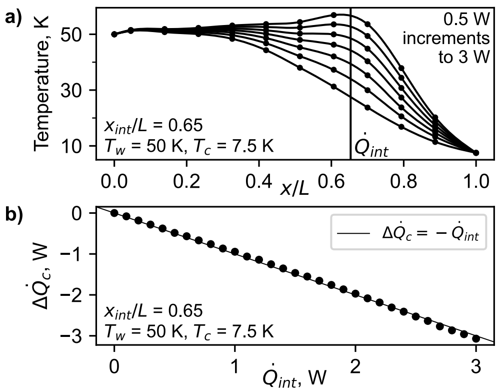

Fig. 6. Intermediate heat injection at a relatively high cold end temperature. a) Temperature profile evolution as intermediate heat is injected at x_{int}/L = 0.65 while T_c = 7.5 K. Bottom profile is with $\dot{Q}_{int}$ = 0 W and higher profiles are with $\dot{Q}_{int}$ increasing by 0.5 W up to 3 W. Profiles are cubic spline fits to temperature readings for only one side of the regenerator; it is appropriate to ignore the other side of the regenerator in this case because the asymmetry is very small once dT_m/dx is large at the cold end [12]. b) The change in $\dot{Q}_c$ for the experiment described in a).

Let us summarize the overall shape of $T_m(x)$ in the absence of intermediate heat, which was studied in [17]. The shape of the temperature profile—either normal, as in Fig. 4, or inverted, as in Fig. 6a—is determined by the difference between the non-temperature-gradient power terms at the warm and cold ends. If $\dot{H}_\beta + \dot{H}_\epsilon + \dot{H}_m$ is greater at the cold end than at the warm end, then the profile may be relatively flat at the cold end, and a significant temperature gradient (transporting power through $\dot{H}_{\nabla T}$) may be required at the warm end to keep $\dot{H}_{2,w} = \dot{H}_{2,c}$. This condition is usually met when T_c is near 4 K because the power due to finite-heat-capacity effects and (especially) real-fluid effects is large, approaching $\dot{E}_{2,c}$ (Fig. 1). At higher T_c, the heat capacity of regenerator materials compared to helium increases ($\dot{H}_\epsilon$ decreases), the importance of real-fluid effects diminishes ($\dot{H}_\beta$ decreases), and the profile may invert. The materials used in regenerator construction, amount of streaming, and end temperatures determine if profile inversion takes place.

3.2. Detailed intermediate cooling capacity maps

Next, we create a comprehensive experimental map of the regenerator's capacity to absorb $\dot{Q}_{int}$, primarily focusing on conditions where $\dot{Q}_c$ is not significantly affected. Up to 3 W is separately applied to each of the 10 heater locations in 0.1 W increments, and the temperature of heat injection T_{int} is measured while T_c is fixed at 3 K and T_w is regulated to 42 K, 50 K, or 58 K.

Fig. 7a-c shows the resulting $T_{int}(\dot{Q}_{int})$ with separate curves for each x_{int}/L. Heater temperature is generally less sensitive to $\dot{Q}_{int}$ when applied to the colder half of the regenerator. At many locations, this sensitivity starts low and then abruptly becomes much higher (as was also observed in [5]). The high-resolution temperature profile measurements of this study reveal additional detail of $T_{int}(\dot{Q}_{int}, x_{int}/L)$—the sensitivity is low when the injection point is near T_c or T_w, and sensitivity is high when heat is applied where dT_m/dx is large. In Section 4, we develop a model to explain $T_{int}(\dot{Q}_{int}, x_{int}/L)$ and the aforementioned changes in sensitivity.

Depending on T_w, cooling power at the cold end slightly decreases or increases as intermediate heat is applied (Fig. 7d-f). However, changes to $\dot{Q}_c$ are usually only a few percent of the original cooling power, even with multiple watts of intermediate heat applied. At a critical value of intermediate heat, the temperature profile may change abruptly—from normal (as in Fig. 4) to inverted (as in Fig. 6a)—and $\dot{Q}_c$ may drop to zero. This is indicated in Fig. 7 by termination of the line for that x_{int}/L. The large decrease in $\dot{Q}_c$ for small changes in $\dot{Q}_{int}$ is a result of the large, sudden increase to $\dot{H}_{2,c}$ that may occur if the temperature gradient reaches the cold end. If the temperature profile of other PTRs does not suddenly invert for high $\dot{Q}_{int}$ (we hypothesize that this is dependent upon the regenerator materials), the sudden decrease to $\dot{Q}_c$ should not occur. Temperature profile changes to high amounts of $\dot{Q}_{int}$ are discussed further in Section 5.2.

Regardless of the value of T_w, $\dot{Q}_{int}$ always decreases the cooling power available at the first stage (Fig. 7g-i). In a typical DIPTR network, the acoustic power flowing from the first-stage regenerator splits between the second-stage regenerator and the first-stage buffer tube, so it is difficult to quantitatively explain the drop in $\dot{Q}_w$ without additional measurements.

Fig. 8a shows a more detailed view of heater temperature vs $\dot{Q}_{int}$. Injections at and past $x_{int}/L = 0.65$ have very similar temperature responses; however, the response of $\dot{Q}_c$ differs. Fig. 8b shows that $\dot{Q}_c$ substantially decreases with increasing $\dot{Q}_{int}$ for injections at $x_{int}/L = 0.84$ and 0.93. This behavior indicates that some of $\dot{Q}_{int}$ is being directed to the cold heat exchanger instead of the warm heat exchanger.

This observation is supported by careful measurements of $T_m(x)$ near the cold heat exchanger. The inset in Fig. 8b shows the temperature difference between the cold heat exchanger and $x_{int}/L = 0.89$ (the thermometer closest to the cold end). The negative values here show that when heat is applied at locations x_{int}/L = 0.84 and 0.93, a negative temperature gradient develops at the cold end. This temperature gradient drives extra power toward the cold heat exchanger, so $\dot{H}_{2,c}$ becomes greater than $\dot{H}_{\beta,c} + \dot{H}_{\epsilon,c}$. The analysis given in Section 3.1 is no longer entirely valid when heat is injected too close to the cold end, and $\dot{Q}_c$ decreases significantly.

4. Temperature profile model

The following section develops an approximate framework for understanding how much intermediate heat may be applied to the regenerator and for predicting the temperature of heat injection. We model the response of the temperature profile to intermediate heat using conservation of total power. The model is composed of two different solutions: a low-temperature solution that is nominally equal to T_c in the base state ($\dot{Q}_{int} = 0$), and a high-temperature solution that is a second-order Taylor-series approximation beginning at T_w. The high and low-temperature solutions are extended from their respective heat exchangers and intersect, giving an approximation to the complete temperature profile.

4.1. Low-temperature solution

At low temperatures (near 4 K), the dominant power terms only depend on T_m, i.e., not on dT_m/dx or other higher-order derivatives. When $\dot{Q}_{int} = 0$, the low-temperature solution is $T_m(x) = T_c$, which has constant total power and matches the boundary condition at the cold end of the regenerator. When $\dot{Q}_{int} > 0$, $\dot{H}_2$ decreases near the point of heat injection according to Eq. (6). Previously [9], we estimated that $\dot{Q}_{int}$ is absorbed into this second-stage regenerator over a distance of about $0.15L$ on either side of the point of heat injection; however, upon further inspection of Fig. 4, most of the temperature profile upstream of heat injection is flat, suggesting $\dot{H}_2$ changes little in that region. We therefore proceed by estimating $\dot{Q}_{int}$ to be absorbed evenly over a distance of $0.15L$ only downstream of heat injection, i.e. towards the cold end.

In this region of heat injection, the change in $T_m(x)$ can be computed from conservation of total power

$$\frac{d\dot{H}_2}{dx} = \left(\frac{d\dot{H}_\beta}{dT_m} + \frac{d\dot{H}_\epsilon}{dT_m} + \frac{d\dot{H}_m}{dT_m}\right)\frac{dT_m}{dx} \approx \frac{\dot{Q}_{int}}{0.15L}, \tag{7}$$

where we have included only the dominant power terms at low temperature.

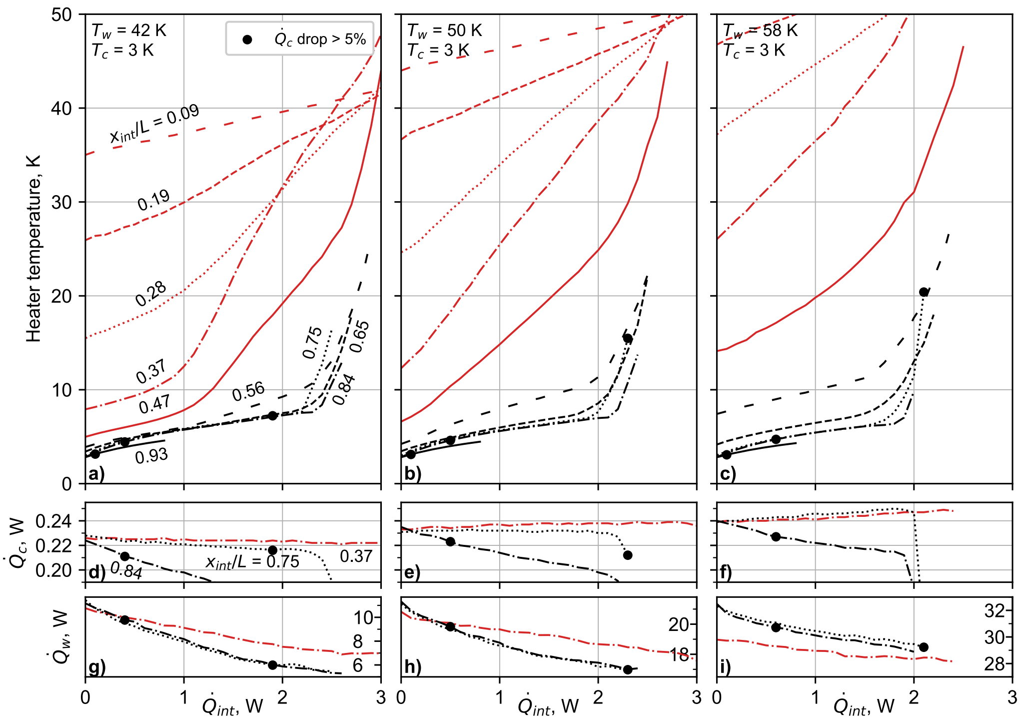

Fig. 7. a-c) The temperature of heat injection for all 10 heater x_{int}/L locations vs the amount of heat injected $\dot{Q}_{int}$. Columns are sorted by regulated warm end temperature. Line style and color key are given in a) and are consistent throughout all subfigures. d-f) Cooling power at the cold end $\dot{Q}_c$ vs $\dot{Q}_{int}$ for x_{int}/L = 0.37, 0.75, and 0.84. These three cases represent the three types of observed behavior. Generally, $\dot{Q}_c$ changed by less than 5% as $\dot{Q}_{int}$ was applied, except when heat was applied very close to the cold end ($x_{int}/L \geq 0.84$) or when $\dot{Q}_{int}$ reached a critical value, as shown by line-termination (higher $\dot{Q}_{int}$ causes $\dot{Q}_c$ to collapse to zero). At small x_{int}/L and low T_w, $\dot{Q}_c$ decrease was negligible for up to 3 W of heat applied, as shown in d) and e) for the x_{int}/L = 0.37 curves. For high T_w (58 K), $\dot{Q}_c$ slightly increases with $\dot{Q}_{int}$ if heat is not applied too near to the cold end, as shown in f). g-i) Cooling power at the regenerator warm end $\dot{Q}_w$ vs $\dot{Q}_{int}$ for the same x_{int}/L values. The drop in $\dot{Q}_w$ is qualitatively consistent with the change in total power in the second-stage regenerator; however, quantitative understanding requires accounting for power changes elsewhere in the DIPTR acoustic network, such as through the first-stage regenerator and buffer tube. The mean pressure at T_w = 42 K, T_c = 3 K, and no intermediate heat—p_{m0}—was 1.24 MPa. The effect of mean pressure on intermediate cooling capacity is discussed in Supplementary 3.

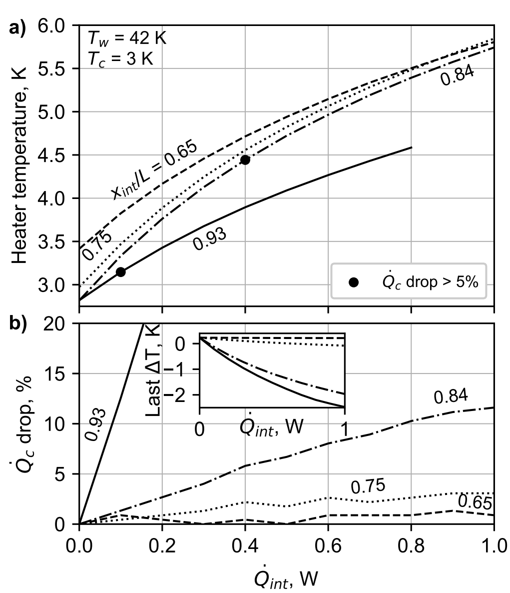

Fig. 8. a) A detailed view of heater temperature vs intermediate heat for the four injection locations closest to the cold end. Line-termination shows where higher $\dot{Q}_{int}$ would cause $\dot{Q}_c$ to be zero. Filled circles indicate where $\dot{Q}_c$ has dropped by at least 5%. b) Drop in $\dot{Q}_c$ as a function of intermediate heat $\dot{Q}_{int}$. Inset shows the temperature difference between the thermometer placed on the cold heat exchanger and the regenerator thermometer closest to the cold end (at $x_{int}/L = 0.89$). Line style is consistent throughout subplots. The mean pressure with no intermediate heat was 1.24 MPa.

Equation (7) can be integrated[9] from the cold end towards the warm end to solve for $T_m(x)$ once the temperature derivatives of the power terms are known. A useful preliminary result for finding these derivatives is Eq. (C.4) from Appendix C:

$$\frac{d\dot{E}_2}{dT_m} = \frac{\beta \dot{E}_2}{1+\epsilon_r}. \tag{8}$$

Using Eq. (8), we compute the temperature derivatives of the power components in Eq. (7) as

$$\frac{d\dot{H}_\beta}{dT_m} = \dot{E}_2 \left[\frac{(1-T_m\beta)\beta}{1+\epsilon_r} - \frac{d(T_m\beta)}{dT_m} \right], \tag{9}$$

$$\frac{d\dot{H}_\epsilon}{dT_m} = \dot{E}_2 T_m \beta \left(\frac{\epsilon_r}{1+\epsilon_r} \right) \left[\frac{1}{T_m\beta}\frac{d(T_m\beta)}{dT_m} + \frac{\beta}{1+\epsilon_r} + \frac{1}{\epsilon_r(1+\epsilon_r)}\frac{d\epsilon_r}{dT_m} \right], \tag{10}$$

$$\frac{d\dot{H}_m}{dT_m} = \dot{N} m c_p, \tag{11}$$

where m is the molar mass of the fluid. The above derivatives govern the change in the temperature profile when intermediate heat is applied near the cold end. Using the methodology developed in Appendix B, we estimate $\dot{N}$ in this regenerator to be approximately 5 mmol/s, which implies $d\dot{H}_m/dT_m$ is about 40 mW/K at 3 K. In contrast, Fig. 4 shows that when $\dot{Q}_{int}$ = 2 W was applied at $x_{int}/L = 0.75$, the temperature rise

[9] Since the power components in Eq. (7) only depend on T_m and not dT_m/dx or higher-order derivatives, Eq. (7) could be solved directly for $\dot{H}_2(x)$. Then, a simple algebraic relationship would give an implicit solution $x(T_m)$. We take the alternative approach described in Section 4 because it gives an explicit solution $T_m(x)$ and it provides several preliminary results we will need for the high-temperature solution in Section 4.2.

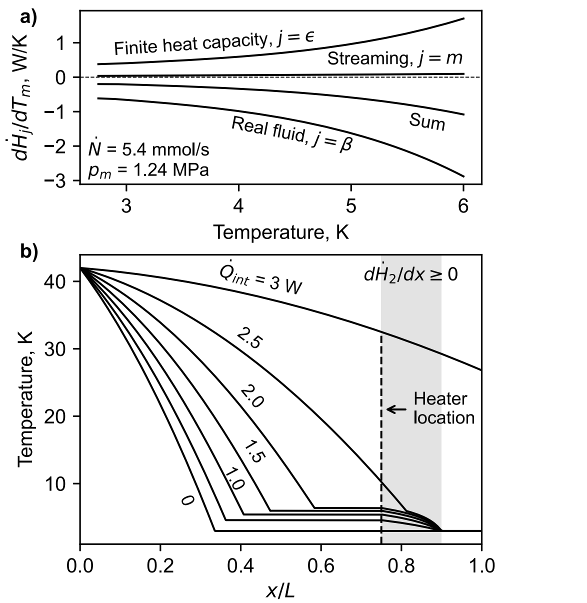

Fig. 9. a) The temperature derivatives of $\dot{H}_\beta$, $\dot{H}_\epsilon$, $\dot{H}_m$, and their sum, which determines the temperature response to intermediate heat for the low-temperature solution. The derivative $d\dot{H}_\epsilon/dT_m$ plotted here was calculated for a regenerator material commonly used in 4 K PTRs. When integrating Eq. (7), we use ϵ_r and associated $d\dot{H}_\epsilon/dT_m$ for the regenerator material at each x. b) The temperature profiles produced by the model for one heat injection location, at x_{int}/L = 0.75. The total heat added ($\dot{Q}_{int}$) is distributed across the shaded region of length $0.15L$ downstream of the heater location. For all subfigures p_m = 1.24 MPa.

at the point of heat injection was 4.5 K, so the measured $d\dot{H}_2/dT_m$ is closer to 440 mW/K. Hence, streaming in this DIPTR only plays a minor role in the low-temperature solution, and most of the temperature response is determined by $d\dot{H}_\beta/dT_m + d\dot{H}_\epsilon/dT_m$.

It may be surprising that $d\dot{H}_\beta/dT_m$ depends on the heat capacity of the regenerator material when $\dot{H}_\beta$ itself is only a function of fluid properties; however, Eq. (8) is responsible for the connection. The overall scale of $d\dot{H}_\beta/dT_m$ and $d\dot{H}_\epsilon/dT_m$ is set by $\dot{E}_2$—higher acoustic power leads to larger temperature derivatives and smaller increases in heater temperature for a given amount of injected heat. The dependence on ϵ_r ensures that different regenerator materials will produce varying T_{int}-$\dot{Q}_{int}$ sensitivities even for regenerators with identical dimensions and acoustic power.

To compare their relative effect on $T_m(x)$, Eqs. (9) to (11) and their sum are plotted in Fig. 9a for the parameters of the regenerator studied here. Because we will integrate the temperature profile from the cold end towards the warm end, $\dot{Q}_{int}$ causes $\dot{H}_2(x)$ to locally drop, so a negative value in Fig. 9a corresponds to a temperature rise with intermediate heat. If a solid material with infinite heat capacity were used ($\epsilon_r \to 0$), $d\dot{H}_2/dT_m$ at the cold end could be approximated by just $d\dot{H}_\beta/dT_m$, which corresponds to the "Real fluid" curve in Fig. 9a.

For the regenerator solid material used here, the "Finite heat capacity" curve in Fig. 9a shows that $d\dot{H}_\epsilon/dT_m$ is positive. The sum of the derivatives is still negative, but its magnitude is smaller than $d\dot{H}_\beta/dT_m$ alone—T_m still rises at the heat injection point, but finite solid heat capacity causes the temperature at the point of heat injection to be more sensitive to intermediate heat. The contribution of streaming ($d\dot{H}_m/dT_m$) is small in this example but could be larger in other systems.

Returning to Eq. (7), we derive the low-temperature solution by integrating dT_m/dx from $x/L = 1$ towards the warm end. The results for multiple values of $\dot{Q}_{int}$ injected at $x_{int}/L = 0.75$ are shown in Fig. 9b as the portions of the curves that extend from $x/L = 1$ to the kinks where the low-temperature solution meets the high-temperature solution.

For injection locations near the cold end (e.g., $x_{int}/L \geq 0.65$), integration of the low-temperature solution produces T_{int} that is close to that observed experimentally. However, for x_{int}/L nearer the middle of the regenerator, the model does not account for T_{int} starting significantly above T_c even with $\dot{Q}_{int} = 0$, so we were forced to start the integration not at T_c but at the experimentally measured $T_{int}(\dot{Q}_{int} = 0)$. The low-temperature part of the model is most useful for x_{int}/L where $T_m(x) \approx T_c$ without intermediate heat applied.

4.2. High-temperature solution

At the warm end, the $|U_1|^2 dT_m/dx$ term ($\dot{H}_{\nabla T}$) in Eq. (2) is significant, and it is difficult to predict the temperature profile without complete numerical models such as REGEN, DeltaEC, and Sage (two of which are considered in Supplementary 1). Instead of pursuing an exact solution, in this section we use a second-order Taylor series expansion to approximate the temperature profile as it extends away from $x = 0$ toward the cold end. Such an approximation cannot predict the complexity of the real temperature profile and is not as accurate as the low-temperature solution; however, it is useful because it leads to simple analytical results which guide our understanding of the response of the regenerator to intermediate heat.

The complete analytical model abruptly transitions from the high-temperature solution to the low-temperature solution where the two intersect. For some values of $\dot{Q}_{int}$, T_w, and T_c, the high-temperature solution may not intersect with the low-temperature solution before x/L = 1. In these cases, the model predicts that these combinations of $\dot{Q}_{int}$, T_w, and T_c cannot be sustained. In the experiment, this corresponds to the second-stage regenerator not being able to maintain T_c at its cold end, even for $\dot{Q}_c$ = 0.

The Taylor series approximation to the temperature profile at the warm end is

$$T_m(x) \approx T_w + \left.\frac{dT_m}{dx}\right|_0 x + \frac{1}{2}\left.\frac{d^2T_m}{dx^2}\right|_0 x^2, \tag{12}$$

where the gradient and curvature of T_m at the warm end are as yet unknown. The gradient at the warm end is determined from the power conservation in Eq. (6):

$$\left.\frac{dT_m}{dx}\right|_0 = \frac{1}{f_{2,w}}\left[\left(1 - \frac{T_c\beta_c}{1+\epsilon_{r,c}}\right)\dot{E}_{2,c} - \left(1 - \frac{T_w\beta_w}{1+\epsilon_{r,w}}\right)\dot{E}_{2,w} - \dot{N}m(h_w - h_c) - \dot{Q}_{int}\right], \tag{13}$$

where subscripts c and w represent evaluation at the cold and warm ends, respectively. In the above, Eq. (2) was used to evaluate $\dot{H}_{2,c}$ and $\dot{H}_{2,w}$, $dT_m/dx|_0$ was isolated from $\dot{H}_{\nabla T,w}$, $\dot{H}_\beta + \dot{H}_\epsilon$ was simplified as $[1 - T_m\beta/(1+\epsilon_r)]\dot{E}_2$, and

$$f_2 = -\frac{\rho_m c_p |U_1|^2}{2\omega A_g(1+\epsilon_r)}\left(\frac{r_h}{\delta_\kappa}\right)^2, \tag{14}$$

which is only valid when evaluated near T_w (see Eq. (A.19) for the definition of f_2 at other temperatures). The coefficient f_2 is always negative.

For T_c = 3 K and with low to moderate amounts of intermediate heat, the bracketed term in Eq. (13) is positive and $dT_m/dx|_0$ negative. An increase in $\dot{Q}_{int}$ lessens the magnitude of the bracketed term and therefore makes a positive contribution to dT_m/dx which extends the high-temperature solution further along the x/L axis, consistent with the experimental observation in Fig. 4. The bracketed term may be used as a very rough metric for the amount of intermediate cooling available before the cold end can no longer be regulated at T_c: once $\dot{Q}_{int}$ increases enough to make $dT_m/dx|_0 = 0$, the high-temperature solution never decreases towards T_c.

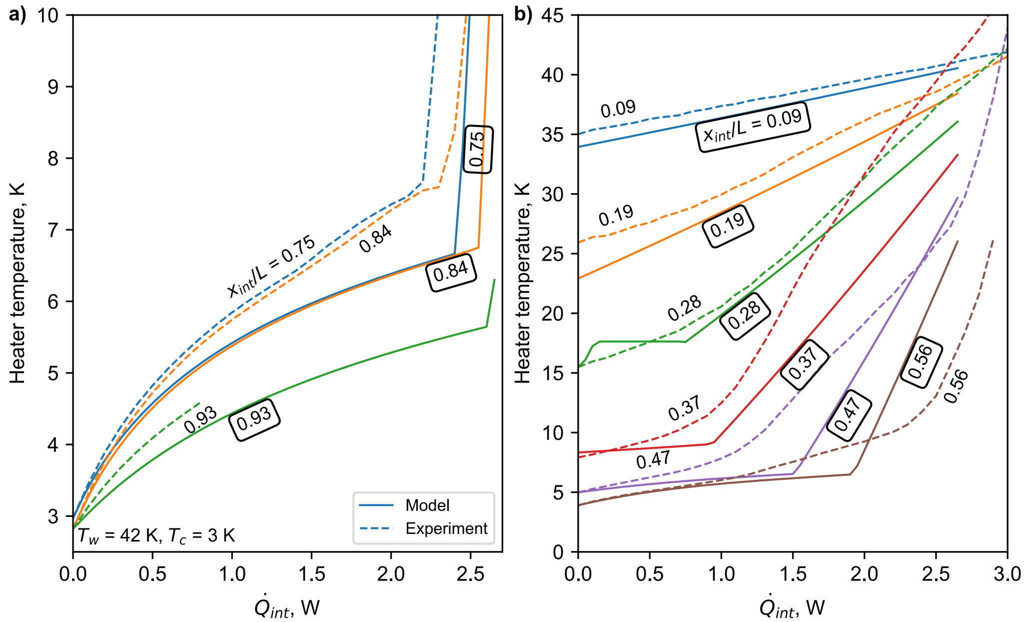

Fig. 10. Modeled (solid lines) and experimentally observed (dashed lines) heater temperatures vs $\dot{Q}_{int}$ for several injection locations. The experimental data is the same as in Fig. 7a. a) Shows injections locations $x_{int}/L \geq 0.75$, while b) shows injections locations $x_{int}/L \leq 0.56$. Data for $x_{int}/L = 0.65$ are excluded for overall figure clarity. The low-temperature solution of the model started integration at the experimentally measured temperature at each heater when no heat was applied. For the modeled results, the high-temperature solution does not intersect the low-temperature solution before $x/L = 1$ for $\dot{Q}_{int} > 2.65$ W, which is why the solid lines end at that heat value. Line ends for the experimental data show the highest amount of intermediate heat before $\dot{Q}_c$ collapses to zero. For the modeled results, p_m = 1.24 MPa, and for all experimental data p_{m0} = 1.24 MPa, where p_{m0} is the mean pressure at T_w = 42 K, T_c = 3 K, and no intermediate heat. The modeled result for x_{int}/L = 0.28 has a plateau at 17.7 K because at that temperature the sum of $d(\dot{H}_\beta + \dot{H}_\epsilon + \dot{H}_m)/dT_m$ becomes positive and the low temperature solution then requires a decrease in temperature as the profile is integrated towards the warm end; the low-temperature part of the model is not accurate at x_{int}/L so far from the cold end where $T_m(x) >> T_c$ and $\dot{H}_{\nabla T}$ is significant.

To make progress with this model we will approximate p_1 and U_1 as real,[10] and then $|U_1|^2 \approx (2\dot{E}_2/p_1)^2$. Acoustic power at any regenerator temperature can be estimated using $\dot{E}_{2,c}$, as discussed in Appendix C, and f_2 is then calculated as

$$f_2 \approx -\frac{(c_p r_h \rho_m \dot{E}_2)^2}{A_g k(1+\epsilon_r)p_1{}^2}. \tag{15}$$

An approximate value for p_1 is obtained using the high-side and low-side pressure gauges of the compressor.[11] Acoustic power at the cold end is estimated from measurements of $\dot{Q}_c$ using Eq. (5), as explained in Appendix B. We are unable to publish the hydraulic radius and other regenerator material properties, but these values are known to us. Commonly used regenerator materials and packing arrangements are discussed in [22].

If the $\dot{Q}_{int}$ injection point is far enough from the warm end at $x/L = 0$, then $d\dot{H}_2/dx|_0 = 0$ and the curvature of the temperature profile at the warm end is

$$\left.\frac{d^2T_m}{dx^2}\right|_0 = \frac{-1}{f_{2,w}}\left[\left(\frac{d\dot{H}_\beta}{dT_m}+\frac{d\dot{H}_\epsilon}{dT_m}+\frac{d\dot{H}_m}{dT_m}\right)\frac{dT_m}{dx}+\frac{df_2}{dT_m}\left(\frac{dT_m}{dx}\right)^2\right]\Bigg|_0. \tag{16}$$

The expressions for $dT_m/dx|_0$ and $d^2T_m/dx^2|_0$ in Eqs. (13) and (16) are substituted into Eq. (12), and the high-temperature solution is extended from $x/L = 0$ towards $x/L = 1$. The results for multiple values of $\dot{Q}_{int}$ injected at $x_{int}/L = 0.75$ are shown in Fig. 9b as the portion of the curves that extend from $x/L = 0$ to the kink where the high-temperature solution meets the low-temperature solution (Section 4.1). High values of $\dot{Q}_{int}$ (e.g., $\dot{Q}_{int}$ = 3 W in Fig. 9b) flatten $dT_m/dx|_0$ so much that the high-temperature solution does not intersect the low-temperature solution before x/L =1. The model cannot satisfy the boundary condition of $T_m = T_c$ at x/L = 1, and these high values of $\dot{Q}_{int}$ cannot be supported.

4.3. Response of $T_m(x)$ to $\dot{Q}_{int}$: experiment vs model

We now compare results of the model to the experimental data presented in Section 3.2. The model was used to compute $T_m(x)$ and the temperature at the injection point using the experimental conditions shown in Fig. 7a. The two results are compared in Fig. 10. For clarity of Fig. 10, the data at x_{int}/L = 0.65 are omitted, although the agreement between data and model for this injection point is similar to the data at $x_{int}/L = 0.75$.

For $\dot{Q}_{int}$ = 0, locations with $x_{int}/L \geq 0.47$ are solidly in the low-temperature solution. As $\dot{Q}_{int}$ begins to increase above zero, the experiment and model are in good agreement for $\dot{Q}_{int}$ up to about 0.5 W. At higher $\dot{Q}_{int}$, the model predicts the temperature of heat injection to be too low. This possibly suggests that the sum of the temperature derivatives plotted in Fig. 9a is too negative, which could occur if our estimate for $\dot{E}_{2,c}$ were too high. Another possible explanation is that the core of the regenerator is significantly colder than the temperature measured on its stainless steel shell—a topic we have not yet investigated since it would require embedding a temperature sensor in the regenerator matrix.[12] However, the experiment-model agreement is still fairly accurate given the complexity of the calculation: for $\dot{Q}_{int}$ = 2 W at x_{int}/L

[10] We usually treat p_1 as real because this phasor does not rotate significantly through the regenerator of interest. For sufficient acoustic power in the regenerator, U_1 should then be mostly real and $(\mathrm{Re}[U_1])^2 >> (\mathrm{Im}[U_1])^2$, so $|U_1|^2 \approx (\mathrm{Re}[U_1])^2$.

[11] In experiments conducted after this study, we instrumented the PTR with pressure sensors at multiple cold head locations. From these measurements—and with the cold end near 4 K—we estimate p_1 in the regenerator to be only 79% of the pressure oscillation as measured by the compressor inlet and outlet. This correction was applied to all p_1 reported in this manuscript.

[12] REGEN3.3 (Supplementary 1) also predicts lower heater temperature compared to experiment, which corroborates this hypothesis.

$= 0.75$, the experimental result is a heater temperature of 7.4 K, while the model predicts 6.4 K.

For $x_{int}/L \geq 0.47$, further increases in $\dot{Q}_{int}$ result in a transition in both the experimental data and the model results from a relatively insensitive response to $\dot{Q}_{int}$ to a much more sensitive response. In Fig. 10, the transition is indicated by a kink in the model results and a more gradual increase in slope in the experimental data. In both cases, this transition occurs when the reduction in $\dot{H}_{2,w}$ (due to increasing $\dot{Q}_{int}$) has sufficiently flattened the temperature profile at $x/L = 0$ so the high-temperature solution extends to the injection point. Sensitivity of heater temperature to $\dot{Q}_{int}$ can then be high because small changes to $dT_m/dx|_0$ cause large changes to the profile far from $x/L = 0$. Before the transition and at injection points $x_{int}/L \geq 0.47$, the heater temperature is determined only by the low-temperature solution—which has relatively shallow slope—explaining the low sensitivity to $\dot{Q}_{int}$.

The model captures the essential aspects of the experimental observations—the transition between low and high-sensitivity regions in $\dot{Q}_{int}$. The relatively poor quantitative agreement between the experiment and model near this transition is to be expected because the intersection happens at low temperatures relative to T_w, where the Taylor-series expansion is not expected to be very accurate.[13]

The heater locations $x_{int}/L = 0.09$ and 0.19 are solidly in the high-temperature solution, even for $\dot{Q}_{int} = 0$. For these data, agreement with the model is quite good. As expected, agreement is poorer as the injection location moves further away from the warm end, since the accuracy of the Taylor-series expansion worsens farther from $x/L = 0$.

5. Direction of intermediate heat flow

In this section, we explore and contrast the general qualities of the temperature profile $T_m(x)$ for moderate and high $\dot{Q}_{int}$. Under the moderate $\dot{Q}_{int}$ heat injections considered so far, $\dot{Q}_{int}$ reduces $\dot{H}_{2,w}$, i.e., the total power between warm end of the regenerator and the injection point. Since T_w is regulated in our experiments, a decrease in $\dot{H}_{2,w}$ requires a reduction in the magnitude of $dT_m/dx|_0$. This results in the high-temperature profile pushing further out toward the cold end, but not so far that $\dot{H}_{2,c}$ is affected. At higher amounts of $\dot{Q}_{int}$, the high-temperature profile eventually encroaches on the cold end and finally creates a finite $dT_m/dx|_L$ (i.e., a negative temperature gradient at the cold end), which increases $\dot{H}_{2,c}$ and decreases $\dot{Q}_c$.

Most experiments reported so far were conducted with $T_c = 3$ K. To better reveal effects at high $\dot{Q}_{int}$, we now consider a set of experiments shown in Fig. 11 with $T_c = 6$ K. This is required because finite $dT_m/dx|_L$ in this PTR can overwhelm all cooling power available at T_c near 3 K. Fig. 11a shows $\dot{Q}_c$ vs $\dot{Q}_{int}$ injected at $x_{int}/L = 0.65$ as $\dot{Q}_{int}$ is swept from 0 W to 3.3 W in 0.1 W increments. Fig. 11b shows the accompanying measured $T_m(x)$. For $\dot{Q}_{int} \leq 2$ W (black data points and curves), $\dot{Q}_c$ stays nearly constant while $dT_m/dx|_L \sim 0$, both implying a fixed $\dot{H}_{2,c}$. For these conditions, Eq. (6) shows that $\dot{Q}_{int}$ creates an equal reduction in $\dot{H}_{2,w}$.

For $\dot{Q}_{int} > 2$ W (blue and red data points and curves), the high-temperature $T_m(x)$ solution reaches $x/L = 1$, creating a finite $dT_m/dx|_L$, which increases $\dot{H}_{2,c}$ and decreases $\dot{Q}_c$. Once $\dot{Q}_{int} \geq 2.3$ W (red data points and curves), Fig. 11a shows that $\dot{Q}_c$ is reduced in equal increments with $\dot{Q}_{int}$. This is an important observation because Eq. (6) then requires that $\dot{H}_{2,w}$ is fixed. This conclusion is consistent with the behavior of the measured $T_m(x)$ near $x/L \sim 0$, as shown in the inset of Fig. 11b, i.e., T_w is fixed and $dT_m/dx|_0$ is nearly constant and approximately zero.

A consistent explanation of this behavior requires a deeper understanding of $\dot{H}_2$ and $T_m(x)$ for both moderate and large values of $\dot{Q}_{int}$.

[13] Note that the high-temperature solution is based on the regenerator properties at $x/L = 0$ and does not account for changes in solid heat capacity or hydraulic radius when the regenerator transitions to other regenerator materials.

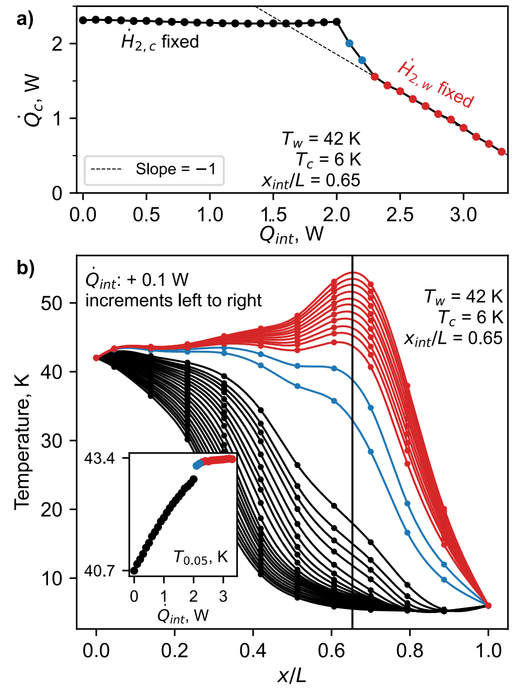

Fig. 11. Large amounts of intermediate heat push the temperature gradient from the warm end to the cold end. a) Cooling power under the conditions shown while intermediate heat was swept between 0 W and 3.3 W in 0.1 W increments. The dashed line has a slope of −1, showing the region where decreases to $\dot{Q}_c$ equal increases to $\dot{Q}_{int}$. The dot colors correspond to the colors of the temperature profiles shown in b) for the same experiment. The blue lines show the profiles when $\dot{Q}_{int} = 2.1$ W and 2.2 W. These data were obtained without thermometers on both sides, so each profile is the cubic spline fit for just one regenerator side. Vertical line shows where heat was injected. Inset plots the temperature at $x/L = 0.05$, showing that the temperature gradient at the warm end only significantly increases for the black data (when $\dot{H}_{2,c}$ is fixed). For both subplots $p_{m0} = 1.24$ MPa. The dots and lines are grouped black (left), blue (middle), and red (right) for both subplots and the inset.

Key to this understanding is the spatial evolution of $T_m(x)$ given in the simplified form of the total power equation:

$$\dot{H}_2 = \dot{H}_0(T_m) + f_2(T_m)\frac{dT_m}{dx}, \tag{17}$$

where—as discussed in Section 4.2—f_2 is less than zero and is temperature and material dependent. The first term on the right of Eq. (17) is our shorthand for the sum of all non-temperature-gradient power terms:

$$\dot{H}_0 \equiv \dot{H}_\beta + \dot{H}_\epsilon + \dot{H}_m, \tag{18}$$

while the second term is a simplified form of the temperature-gradient-dependent power term $\dot{H}_{\nabla T}$. The conduction power term of Eqs. (2) and (3) is assumed to be insignificant.

In the remainder of Section 5, we discuss the general properties of the $T_m(x)$ solutions to Eq. (17) and how those properties influence the division of $\dot{Q}_{int}$ between the cold and warm ends of the regenerator.[14] Although both $\dot{H}_0$ and f_2 depend on the regenerator matrix material and this material varies within the regenerator, the following analysis takes the simplified approach, neglecting the material transitions.

We have performed a related analysis on the qualitative shape of the temperature profile but in the absence of intermediate heat [17]. A major conclusion of [17] is that the overall shape of $T_m(x)$ is determined by the quantity $\dot{H}_{0,c} - \dot{H}_{0,w}$. For most of this study that difference has been positive, causing there to be zero temperature gradient at the cold

[14] Supplementary 4 considers how the regenerator material may influence the division of $\dot{Q}_{int}$ between the two ends.

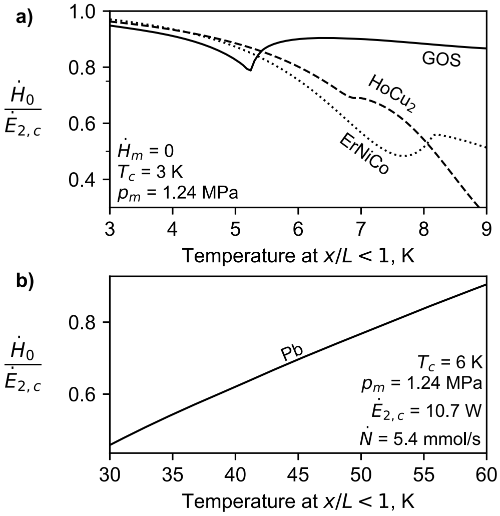

Fig. 12. a) Non-temperature-gradient power terms at temperatures near T_c normalized by acoustic power at the cold end. Steady mass flow power $\dot{H}_m$ was assumed negligible because for the small temperature changes considered here $\Delta\dot{H}_m$ is much less than $\Delta\dot{H}_\beta$ and $\Delta\dot{H}_\epsilon$ (Fig. 9a). While Fig. 1b calculated these power terms at different cold-end temperatures, this plot considers how the terms change within the regenerator as $T_m(x)$ evolves (3 K is the cold end, and higher temperatures represent locations within the regenerator at $x/L < 1$). Therefore, this plot includes the scaling of $\dot{E}_2(T_m)$ which was calculated according to Eq. (C.5); this scaling is unique to each material because of the ϵ_r dependence in Eq. (C.5). b) Non-temperature-gradient power terms at temperatures near T_w normalized by acoustic power at the cold end. Acoustic power at the warm end was calculated assuming a cold end temperature of 6 K and a cold-end acoustic power of 10.7 W, and $\dot{H}_\epsilon$ was calculated using the heat capacity of lead. The steady molar flow rate in this regenerator is estimated to be about 5.4 mmol/s (see Appendix B).

end. However, when that difference is negative the profile can have zero gradient at the warm end and significant gradient at the cold end (Fig. 6a); we call such $T_m(x)$ an "inverted" profile.

5.1. Moderate $\dot{Q}_{int}$ ($\dot{H}_{2,c}$ fixed)

Up to this point (moderate $\dot{Q}_{int}$) we have approximated $dT_m/dx|_L = 0$ and the total power at the cold end $\dot{H}_{2,c} = \dot{H}_0(T_c) \equiv \dot{H}_{0,c}$; however, this cannot be strictly true. If it were, then the solution to Eq. (17) is $T_m(x) = T_c$, which cannot satisfy the $T_m(x=0) = T_w$ boundary condition. Instead, $\dot{H}_{2,c}$ must slightly differ from $\dot{H}_{0,c}$. The following paragraph determines the sign of that difference.

If $\dot{H}_{2,c} < \dot{H}_{0,c}$, then Eq. (17) shows that $dT_m/dx|_L > 0$ and T_m would decrease below T_c moving away from the cold heat exchanger towards the warm end. Fig. 12a shows that $\dot{H}_0 \approx \dot{H}_\beta + \dot{H}_\epsilon$ increases as T_m decreases[15] near T_c; to maintain constant $\dot{H}_2(x)$ as $\dot{H}_0$ increases, dT_m/dx must become more positive (making $f_2 dT_m/dx$ more negative), further decreasing T_m. The temperature dependence of f_2 in Eq. (17) also contributes to the need for dT_m/dx to become more positive for decreasing T_m: near T_c, $|f_2|$ decreases with decreasing T_m (Fig. A.3a). Therefore, if $\dot{H}_{2,c} < \dot{H}_{0,c}$, T_m would decrease exponentially moving away from the cold end toward the warm end, and there is no way to satisfy the $T_m(x=0) = T_w$ boundary condition.

From the discussion above, we can conclude that $\dot{H}_{2,c} > \dot{H}_{0,c}$, $dT_m/dx|_L < 0$, and $T_m(x) > T_c$.[16] As T_m increases moving away from the cold end toward the warm end, Fig. 12a shows that $\dot{H}_0$ decreases, requiring an increase in $f_2 dT_m/dx$ to keep $\dot{H}_2(x)$ constant. This results in $T_m(x)$ increasing exponentially moving away from the cold heat exchanger towards the warm end. This exponential growth (illustrated in the bottom two curves of Fig. S6) transforms very small changes in $\dot{H}_{2,c}$ relative to $\dot{H}_{0,c}$ into large changes in $T_m(x)$ at locations farther from the cold heat exchanger—a conclusion consistent with the behavior of the black data points in Fig. 11a (i.e., nearly fixed $\dot{Q}_c$) and the black $T_m(x)$ curves in Fig. 11b. For moderate $\dot{Q}_{int}$, the exponential growth of $T_m(x)$ in this region is responsible for the nearly fixed $\dot{H}_{2,c} \approx \dot{H}_{0,c}$ because it allows very small changes in $\dot{H}_{2,c}$ to accommodate large changes in $T_m(x)$ and $\dot{H}_{2,w}$ while still satisfying the boundary condition $T_m(x=0) = T_w$. Under these conditions, $\dot{Q}_{int}$ primarily affects the regenerator at locations upstream of heat injection.

5.2. High $\dot{Q}_{int}$ ($\dot{H}_{2,w}$ fixed)

The blue and red data in Fig. 11a and Fig. 11b show that, at higher $\dot{Q}_{int}$ (lower $\dot{H}_{2,w}$), the high-temperature profile reaches the cold end, $dT_m/dx|_L$ is no longer very close to zero, and $\dot{H}_{2,c}$ is no longer very close to $\dot{H}_{0,c}$. The large difference between $\dot{H}_{2,c}$ and $\dot{H}_{0,c}$ reduces the importance of exponential growth of $T_m(x)$ between the cold heat exchanger and the $\dot{Q}_{int}$ injection point. Rather, this growth is dominated by extrapolation of $dT_m/dx|_L$, and relatively larger changes in $\dot{H}_{2,c}$ are needed to create the significant changes in $T_m(x)$ needed to smoothly match up with the high-temperature solution at the $\dot{Q}_{int}$ injection point. Hence, $\dot{H}_{2,c}$ is no longer nearly fixed at $\dot{H}_{0,c}$.

To regain understanding of $\dot{H}_{2,c}$ and $\dot{H}_{2,w}$, we turn our attention to $T_m(x)$ near the warm end of the regenerator. In the moderate range of $\dot{Q}_{int}$ discussed in the previous subsection, $\dot{H}_{2,w}$ is significantly different from (and larger than) $\dot{H}_{0,w}$. Under these conditions, and in analogy with the discussion in the previous paragraph, the evolution of $T_m(x)$ moving away from the warm heat exchanger is dominated by extrapolation of $dT_m/dx|_0$ (black curves in Fig. 11b). The total power at the warm end $\dot{H}_{2,w}$ decreases in nearly[17] equal response to the increases in $\dot{Q}_{int}$, and at a high enough value of $\dot{Q}_{int}$, $\dot{H}_{2,w}$ becomes very close to $\dot{H}_{0,w}$. At this point, the evolution of $T_m(x)$ near $x/L = 0$ transitions to exponential behavior (red curves in Fig. 11b).

The exponential behavior of $T_m(x)$ at the warm end arises in the same way as in Section 5.1 for the cold end, with the key insight that $d\dot{H}_0/dT_m > 0$ at the warm end (Fig. 12b). This leads to the conclusion that $T_m(x)$ increases exponentially with x.

For high $\dot{Q}_{int}$, the roles of the cold and warm ends are reversed relative to moderate $\dot{Q}_{int}$—very small changes in $\dot{H}_{2,w}$ create the significant changes in T_m at the $\dot{Q}_{int}$ injection point and $\dot{H}_{2,w}$ becomes nearly fixed at $\dot{H}_{0,w}$. The changes in T_m at the $\dot{Q}_{int}$ injection point create significant change in dT_m/dx between the injection point and $x/L = 1$, which results in an increase in $\dot{H}_{2,c}$ and nearly all of the additional $\dot{Q}_{int}$ flowing toward the cold end. This discussion is consistent with the red data points in Fig. 11a (where $\Delta\dot{Q}_c \approx -\Delta\dot{Q}_{int}$).

Recall that, near the cold heat exchanger, we concluded $T_m(x) > T_c$ for any value of $\dot{Q}_{int}$. In contrast, near the warm heat exchanger, the in-

[15] For T_m < 5.2 K, this is true for all example materials plotted here. Let us consider a regenerator made with $HoCu_2$ or ErNiCo, since analysis of a regenerator made with GOS is complicated by the fact that $\dot{H}_0$ can both decrease (T_m < 5.2 K) and increase (T_m > 5.2 K) with increasing temperature.

[16] We note that the black curves in Fig. 11b show a slight but consistent decrease in $T_m(x)$ around x/L = 0.9. We believe this is primarily due to an additional physical process for total power not represented in Eq. (17) related to an end effect driven by the non-negligible displacement of the helium fluid parcels and the transition from quasi-isothermal behavior inside the regenerator to quasi-adiabatic behavior outside of the regenerator. The same end effect may be responsible for the behavior at the warm end, where the temperature near x/L = 0.05 can be slightly greater than T_w (Fig. 11b).

[17] Except for the very small changes in $\dot{H}_{2,c}$ needed to drive the changes in the exponential growth of $T_m(x)$ between the cold heat exchanger and the $\dot{Q}_{int}$ injection point.

crease of $T_m(x)$ above T_w is allowed because of the influence of $\dot{Q}_{int}$. For high $\dot{Q}_{int}$ profiles that increase exponentially in temperature (the red curves in Fig. 11b) to satisfy the boundary condition $T_m(x/L = 1) = T_c$, they must pass back through $T_m(x) = T_w$ with $dT_m/dx < 0$, which implies that, at the point of crossing, $\dot{H}_2 > \dot{H}_{2,w} \approx \dot{H}_{0,w}$. This condition can be accommodated, but only at locations between the $\dot{Q}_{int}$ injection point and the cold heat exchanger where $\dot{Q}_{int}$ has increased the total power such that $\dot{H}_2 = \dot{H}_{2,c} = \dot{H}_{2,w} + \dot{Q}_{int} > \dot{H}_{2,w}$. This is consistent with the red curves of Fig. 11b, where the profiles drop below T_w with $dT_m/dx < 0$ at locations always past the vertical line where heat is injected.

At the warm heat exchanger, the transition from the $T_m(x)$-decreasing to $T_m(x)$-increasing behavior (blue to red curves in Fig. 11b) occurs when $\dot{H}_{2,w} = \dot{H}_{0,w}$. This behavior is a potential opportunity to independently measure $\dot{H}_0(T_w)$. However, the transition occurs over a range of $\dot{Q}_{int}$, and additional investigation is needed to determine how best to leverage this behavior.

6. Lessons for cryocooler designers

For heat injection locations closer to the cold end, the data in Fig. 7a-c show a region where the heater temperature is relatively insensitive to $\dot{Q}_{int}$. This temperature stability is potentially useful for thermal integration design, and practitioners may want to maximize the $\dot{Q}_{int}$ span of this region. As discussed in Section 4.3, the transition at the end of this region to a more sensitive temperature response occurs when $\dot{H}_{2,w}$ has been lowered sufficiently (by increases to $\dot{Q}_{int}$) that the warm-end temperature profile finally extends to the injection point. This change in the $T_m(x)$ profile is driven by $dT_m/dx|_0$ becoming less negative, i.e., the temperature profile becomes more flat at the warm end and extends further toward the cold end.

The insensitive region can be extended by moving the heat injection point farther from the warm end so a shallower $dT_m/dx|_0$ (larger $\dot{Q}_{int}$) is needed for the warm-end profile to reach the injection point. Fig. 7a shows that increasing x_{int}/L has a significant effect as the $\dot{Q}_{int}$-insensitive region begins to emerge (0.37< x_{int}/L <0.56); however, at larger x_{int}/L this effect tapers off (e.g., the $\dot{Q}_{int}$-insensitive regime is nearly the same for x_{int}/L = 0.65 and 0.84). This behavior is qualitatively consistent with the relative changes in $dT_m/dx|_0$. If x_0/L is the location where the base $T_m(x)$ profile (with $\dot{Q}_{int}$ = 0) transitions from the high-temperature to low-temperature profiles, then the initial increments in the injection location beyond x_0/L enable the largest changes in $dT_m/dx|_0$ (and $\dot{Q}_{int}$) before the increase in sensitivity. Using a longer second-stage regenerator (assuming that additional viscous losses are not of much consequence) would also allow the injection point to be farther from x_0 before the increase in sensitivity occurs, but this too is subject to diminishing returns, especially as $dT_m/dx|_0$ approaches 0.

Design changes that affect the partitioning of warm-end power between $\dot{H}_\beta$, $\dot{H}_\epsilon$, $\dot{H}_m$, and $\dot{H}_{\nabla T}$ can also extend the $\dot{Q}_{int}$-insensitive region. If $\dot{H}_{\nabla T}$ is a larger fraction of $\dot{H}_{2,w}$, then $dT_m/dx|_0$ becomes more negative and x_0/L is smaller, enabling larger increases to $\dot{Q}_{int}$ before the high-temperature profile reaches the injection point. This effect on the sensitivity of $dT_m/dx|_0$ to $\dot{Q}_{int}$ may also be seen in the model for the high-temperature solution in Section 4.2, specifically the bracketed term in Eq. (13) for $dT_m/dx|_0$. Partitioning more of the power to $\dot{H}_{\nabla T}$ can be achieved in several ways. A reduction in $\dot{H}_\epsilon$ at the warm end is possible by increasing the volumetric heat capacity of the solid (by reducing its porosity or increasing its specific heat). Because acoustic power at the warm end is large ($\dot{E}_{2,w}/\dot{E}_{2,c} > 5$ at T_w = 42 K, T_c = 3 K, and p_m = 1.24 MPa), $\dot{H}_\epsilon$ is significant at the warm end even though ϵ_r there can be quite small. For $\dot{E}_{2,c}$ = 10.7 W, T_w = 42 K, and T_c = 3 K, we estimate that a 20% decrease in ϵ_r at the warm end would decrease $\dot{H}_\epsilon$ (increase $\dot{H}_{\nabla T}$) there by about 0.4 W; the available intermediate cooling in the insensitive regime would increase by the same amount. A reduction in $\dot{H}_{m,w} - \dot{H}_{m,c}$ is possible if $\dot{N}$ could be reduced without negatively impacting performance.[18] Intermediate cooling could be increased by $\dot{N}m(h_w - h_c)$, which is about 0.9 W per mmol/s of steady flow for T_w = 42 K, T_c = 3 K, and p_m = 1.24 MPa. Since streaming through the first-stage regenerator does subtract from the cooling available at T_w [24], this might also have the benefit of increasing cooling power at the warm end.

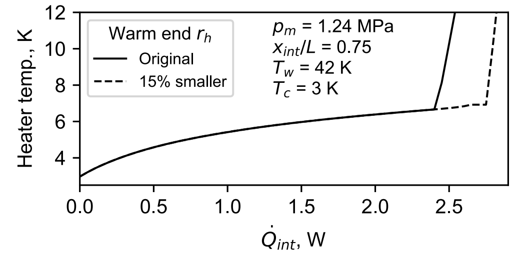

Fig. 13. Heater temperature vs intermediate heat as predicted by the model at an injection location of x_{int}/L = 0.75, showing one example of how regenerator parameters at the warm end impact the available intermediate cooling. Solid line is the result for the original r_h, while the dashed line is the result when r_h was decreased by 15%.

Rather than changing the partitioning between the power terms at the warm end, a similar effect on x_0/L and the span of the $\dot{Q}_{int}$-insensitive region may be achieved by increasing $\dot{E}_{2,c}$. Fig. S5b in Supplementary 3 shows that when the overall scale of power in the regenerator is increased ($\dot{E}_2$ was increased by a 0.25 MPa increase in p_m), so too is the available $\dot{Q}_{int}$. In that example, $\dot{E}_{2,c}$ was increased by an estimated 2.7 W, resulting in an increase of $\dot{H}_{2,c}$ by a similar amount (at 3 K, $\dot{H}_\beta$ alone is 92% of $\dot{E}_{2,c}$). Using Eq. (2), we estimate that $\dot{H}_{\nabla T,w}$ carries an additional 0.6 W of power in the base state ($\dot{Q}_{int} = 0$) for the p_{m0} = 1.24 MPa data compared to the lower pressure p_{m0} = 0.99 MPa data. This result is roughly consistent with the approximately 1 W increase in the $\dot{Q}_{int}$-insensitive region shown in Fig. S5b.

Modification of $f_{2,w}$ in Eq. (13) can also be used to increase the size of the insensitive region. This term is always negative, but by decreasing $|f_{2,w}|$, $dT_m/dx|_0$ is made more negative for a given $\dot{Q}_{int}$. Equation (14) suggests that decreasing the hydraulic radius r_h is perhaps the clearest way to achieve this change. Fig. 13 shows the results of the Section 4 model with fixed parameters besides a 15% decrease in r_h at the warm end of the regenerator. The heater temperature is identical for lower values of $\dot{Q}_{int}$, but the transition to the $\dot{Q}_{int}$-sensitive region occurs near $\dot{Q}_{int}$ = 2.8 W using the smaller r_h vs 2.4 W using the original r_h.

Usually the temperature of the first stage will be set by the specific cryogenic application and its thermal loads; however, minimizing such loads to the greatest degree possible will also increase the available intermediate cooling by depressing T_w. Higher warm-end temperatures lead to smaller $\dot{Q}_{int}$-insensitive regions, as shown in Fig. 7a-c. This is likely related to x_0/L increasing as the first stage rises in temperature.

7. Conclusion and summary

The first studies demonstrating intermediate cooling in 4 K PTR regenerators are about two decades old; however, there is still much to learn about the mechanisms and limits of this cooling source. The insights and analysis in this manuscript should help cryocooler manufacturers design systems that utilize all the cooling power available from these machines. Better utilization of intermediate cooling enables current systems to accommodate larger heat loads and allows smaller coolers to perform the same function as larger ones, lowering infrastructure requirements such as space, electricity, and water.

[18] Streaming from the warm end to the cold end of the regenerator has been shown to increase the cooling power at the second-stage heat exchanger [23], most likely by reducing parasitic heat loads from the thermal buffer tube.

Modern computer codes (REGEN 3.3, Sage, and DeltaEC) include the physics on which Eq. (2) is based, and can accurately predict the performance of cryocoolers (Supplementary 1). However, simplifying approximations and separate consideration of the terms in Eq. (2) yield better understanding, and thus can lead to insights about performance improvements. For example, in Section 6 simple analysis showed that small changes to regenerator design can have significant changes to the amount of intermediate cooling available. It is a noteworthy insight that regenerator characteristics at the warm end limit this source of cooling.

We summarize the findings of this manuscript below:

1. (Fig. 1) The pressure dependence of enthalpy in the real-fluid regime—and to a lesser extent finite solid heat capacity—determines the power flow through 4 K cryocooler regenerators and severely limits cold-end cooling power.
2. (Fig. 1, Fig. 9) Intermediate heat injection barely affects cold-end cooling power because the real-fluid and finite-heat-capacity power terms are very sensitive to temperature near 4 K. Small changes to these terms at the cold end can produce large changes to power at the warm end.
3. (Fig. 6) Intermediate cooling is not available at cold-end temperatures above about 7 K.
4. (Fig. 7) While the analysis developed here applies generally to low-frequency PTRs, experimental results are from a specific commercial DIPTR. Regenerator construction may influence heat injection temperatures, the intermediate cooling available, and the sensitivity of cold-end cooling power.
5. (Fig. 7) Power at the warm end of the regenerator decreases by the amount of intermediate heat applied. There must be flexibility in the temperature profile near the warm end for there to be negligible impact to cold-end cooling.
6. (Fig. 7) First stage cooling power decreases when intermediate heat is applied to the second-stage regenerator; this decrease is similar in size to the intermediate heat.
7. (Fig. 8) Intermediate heat is absorbed into the regenerator over a finite axial distance and therefore should not be injected too close to the cold end.
8. (Fig. 9) The temperature derivatives of the real-fluid and finite-heat-capacity contributions to power determine the temperature of heat injection when heat is applied far from the temperature gradient.
9. (Fig. 9, Fig. 10) The temperature gradient translates towards the cold end with increasing intermediate heat and eventually increases the sensitivity of heater temperature. In this way, conditions at the warm end determine how much intermediate cooling is available.
10. (Fig. 11) When a large amount of heat is applied to the regenerator its temperature profile may invert. Once inverted, increases to intermediate heat are directly parasitic to cold-end cooling while total power at the warm end is fixed.
11. (Fig. 13) Decreasing steady mass flow, increasing acoustic power, and increasing volumetric heat capacity at the warm end are examples of how the available intermediate cooling may be increased through cryocooler design.

We also provide a summary of the appendices and supplementary material:

1. (Appendix A) The total power flow equation is an approximation appropriate for regenerators with hydraulic radius much smaller than the fluid's thermal penetration depth.
2. (Appendix B) Estimates for acoustic power and steady mass flow may be obtained through temperature profile and cooling power measurements.
3. (Appendix C) In the real-fluid regime, acoustic power scales in the regenerator as a function of the thermal expansion coefficient and volumetric specific heat ratio.
4. (Fig. S1) Numerical codes such as REGEN3.3 and DeltaEC are able to simulate regenerator cooling in 4 K PTRs with reasonable accuracy.
5. (Fig. S3) The phase of the flow rate at the cold end of the regenerator influences the available intermediate cooling.
6. (Fig. S5) The charge pressure of low-frequency PTRs strongly impacts the available intermediate cooling through changes to acoustic power.
7. (Fig. S6) Regenerator material selection may influence the sensitivity of cold-end cooling power to intermediate heat.

CRediT authorship contribution statement

Ryan Snodgrass: Conceptualization, Methodology, Investigation, Data Curation, Writing, Visualization. **Gregory Swift**: Conceptualization, Supervision, Writing. **Joel Ullom**: Conceptualization, Supervision, Writing, Funding Acquisition. **Scott Backhaus**: Conceptualization, Methodology, Supervision, Writing.

Declaration of competing interest

The authors declare that they have no known competing financial interests or personal relationships that could have appeared to influence the work reported in this paper.

Data availability

The authors do not have permission to share data.

Acknowledgements

R. Snodgrass acknowledges support from a National Research Council Postdoctoral Fellowship, and from the Professional Research Experience Program (PREP) between the University of Colorado Boulder and NIST under award number 70NANB18H006. Fluid properties were obtained from CoolProp [25]. Manuscript is a contribution of NIST, and not subject to copyright. We acknowledge guidance and advice on the topic of this manuscript from Vincent Kotsubo and Ray Radebaugh of NIST; we would also like to thank Ray for his assistance with the REGEN3.3 model used in this study. Certain equipment, instruments, or materials are identified in this paper in order to specify the experimental procedure adequately. Such identification is not intended to imply recommendation or endorsement by NIST, nor is it intended to imply that the materials or equipment identified are necessarily the best available for the purpose.

Appendix A. Simplifications to the total power equation in the small r_h/δ_κ limit

A.1. Background

Although modern cryocooler regenerators would be most accurately described by the equations for porous media, such equations are difficult to simplify because many parameters are functions of Reynolds number which in turn is a function of time. A more straightforward approach that still captures the important physics is to use the equations for parallel plates. Start with the total power equation given by Swift[19]:

[19] This result can be obtained from Eq. (A30) in [26] by using the spatial average of that paper's Eq. (A4) to eliminate dp_1/dx, adding the $\dot{N}$ term, and changing to our present notation. The final form is also given in [27].

$$\dot{H}_2(x) = \frac{1}{2}\mathrm{Re}\left[p_1\tilde{U}_1\left(1 - \frac{T_m\beta(f_\kappa - \tilde{f}_\nu)}{(1+\epsilon_s)(1+\sigma)(1-\tilde{f}_\nu)}\right)\right] + \frac{\rho_m c_p |U_1|^2}{2\omega A_g(1-\sigma)}\frac{1}{|1-f_\nu|^2}\mathrm{Im}\left[\tilde{f}_\nu + \frac{(f_\kappa - \tilde{f}_\nu)(1+\epsilon_s f_\nu/f_\kappa)}{(1+\epsilon_s)(1+\sigma)}\right]\frac{dT_m}{dx} - (A_g k + A_s k_s)\frac{dT_m}{dx} + \dot{N}mh. \quad (A.1)$$

The goal is to simplify the first two terms of Eq. (A.1). The spatially averaged functions f_κ and f_ν are known for specific regenerator geometries, such as parallel plates or circular pores. The function f_κ captures the thermal contact between the fluid and solid, while f_ν captures viscous effects. More detail can be found in [15]. The thermal and viscous penetration depths are

$$\delta_\kappa = \sqrt{\frac{2k}{\omega\rho_m c_p}}, \quad (A.2)$$

$$\delta_\nu = \sqrt{\frac{2\mu}{\omega\rho_m}}, \quad (A.3)$$

where k is the fluid's thermal conductivity and μ is the fluid's dynamic viscosity. The Prandtl number is $\sigma = (\delta_\nu/\delta_\kappa)^2$.

Porous-media regenerators with porosity ϕ and hydraulic radius r_h are approximated by parallel-plate regenerators with plate spacing $2y_0$ equal to $2r_h$ and plate thickness $2l$ equal to $2r_h(1-\phi)/\phi$. The functions f_j (for $j = \kappa, \nu$) are

$$f_j = \frac{\tanh[(1+i)r_h/\delta_j]}{(1+i)r_h/\delta_j}, \quad (A.4)$$

where $i = \sqrt{-1}$. In low-temperature regenerators, r_h/δ_j is of order 0.1. A Taylor series expansion in the limit of small r_h/δ_j is used to rewrite f_j as:

$$f_j \approx 1 - i\frac{2}{3}\left(\frac{r_h}{\delta_j}\right)^2 - \frac{8}{15}\left(\frac{r_h}{\delta_j}\right)^4 + i\frac{136}{315}\left(\frac{r_h}{\delta_j}\right)^6, \quad (A.5)$$

where terms of order $(r_h/\delta_j)^8$ and higher are neglected. The hydraulic radius is the wetted volume divided by the wetted area. For a regenerator packed with spheres of diameter d the hydraulic radius is

$$r_h = \frac{d}{6}\frac{\phi}{1-\phi}. \quad (A.6)$$

In thermoacoustic analysis, the volumetric ratio of the fluid to solid heat capacities ϵ_s has both real ϵ_r and imaginary ϵ_i components. For the parallel plate geometry, this parameter is

$$\epsilon_s = \frac{\rho_m c_p y_0}{\rho_s c_s l}\frac{f_\kappa}{f_s}, \quad (A.7)$$

$$= \epsilon_r + i\epsilon_i, \quad (A.8)$$

The solid's thermoacoustic function f_s is calculated the same as f_κ except using the thermal conductivity, density, and specific heat of the regenerator solid, and l instead of y_0. In the small r_h/δ_κ limit, ϵ_s is

$$\epsilon_s = \frac{\rho_m c_p y_0}{\rho_s c_s l}\left[1 + \frac{2i}{3}\left(\frac{l^2}{\delta_s^2} - \frac{y_0^2}{\delta_\kappa^2}\right)\right]. \quad (A.9)$$

From Eq. (A.9), we see that the imaginary part of ϵ_s is much smaller than the real component: ϵ_i/ϵ_r is of order $(r_h/\delta_\kappa)^2 \sim 0.01$. The real part of Eq. (A.9) is

$$\epsilon_r = \frac{\phi\rho_m c_p}{(1-\phi)\rho_s c_s}. \quad (A.10)$$

A.2. Simplifying the $p_1\tilde{U}_1$ power term

The expansion Eq. (A.5) is now used to simplify the parts of Eq. (A.1) containing f_j, σ, and ϵ_s. For the $p_1\tilde{U}_1$ term, the quantity of interest is C_{pu}:

$$C_{pu} = \frac{(f_\kappa - \tilde{f}_\nu)}{(1+\epsilon_s)(1+\sigma)(1-\tilde{f}_\nu)}. \quad (A.11)$$

Complex algebra (using SymPy [28]) gives a numerator and denominator which are each a sum of terms of the form ${r_h}^p{\delta_\kappa}^q{\delta_\nu}^r$ where p, q, and r are non-negative integers whose sum is constant for each term. For low-temperature regenerators, we drop terms with $p > 2$, giving

$$C_{pu} \approx \frac{1}{1+\epsilon_s}\frac{5i{\delta_\kappa}^2{\delta_\nu}^2 - 4{\delta_\kappa}^2{r_h}^2 + 4{\delta_\nu}^2{r_h}^2}{{\delta_\kappa}^2\left(5i{\delta_\nu}^2 - 4{r_h}^2\right)}. \quad (A.12)$$

The above is simplified using the complex conjugate and again dropping terms with $p > 2$. The imaginary component of ϵ_s is small compared to the real component, so terms of order ${\epsilon_i}^2$ or order $\epsilon_i(r_h/\delta_\kappa)^2$ are neglected. This yields

$$C_{pu} \approx \frac{1}{1+\epsilon_r} - i\left[\frac{\epsilon_i}{(1+\epsilon_r)^2} + \frac{4{r_h}^2/5{\delta_\kappa}^2}{1+\epsilon_r}\right]. \quad (A.13)$$

The validity of the above approximation is checked using appropriate fluid and solid properties at an operating frequency of 1.4 Hz. Fig. A.1a,b shows that the difference between Eq. (A.11) and Eq. (A.13) is less than 1% for r_h less than 30 μm, which is a reasonable hydraulic radius for these low-temperature regenerators.

The approximation for C_{pu} is inserted back into Eq. (A.1). Using the definition of acoustic power $\dot{E}_2 = \mathrm{Re}[p_1\tilde{U}_1]/2$, the following is obtained for the first term of Eq. (A.1):

$$\frac{1}{2}\mathrm{Re}\left[p_1\tilde{U}_1\left(1 - \frac{T_m\beta(f_\kappa - \tilde{f}_\nu)}{(1+\epsilon_s)(1+\sigma)(1-\tilde{f}_\nu)}\right)\right] \approx \left(1 - \frac{T_m\beta}{1+\epsilon_r}\right)\dot{E}_2 - \frac{T_m\beta}{2}\left[\frac{\epsilon_i}{(1+\epsilon_r)^2} + \frac{4{r_h}^2/5{\delta_\kappa}^2}{1+\epsilon_r}\right]\mathrm{Im}[p_1\tilde{U}_1], \quad (A.14)$$

where the first term of the approximation can also be separated into terms that do and do not contain ϵ_r:

$$\left(1 - \frac{T_m\beta}{1+\epsilon_r}\right)\dot{E}_2 = (1 - T_m\beta)\dot{E}_2 + \frac{\epsilon_r}{1+\epsilon_r}T_m\beta\dot{E}_2. \quad (A.15)$$

We now consider if the second term of the approximation in Eq. (A.14) is of significance or if it can be neglected. In any effective regenerator, $\mathrm{Re}[p_1\tilde{U}_1] > \mathrm{Im}[p_1\tilde{U}_1]$. For convenience, we will here approximate $\mathrm{Re}[p_1\tilde{U}_1] \approx 2\mathrm{Im}[p_1\tilde{U}_1]$ so $\mathrm{Im}[p_1\tilde{U}_1] \approx \dot{E}_2$, and then it is only necessary to compare the sizes of the first and second coefficients of Eq. (A.14). Fig. A.2a shows that the coefficient of the second term is—at maximum—about 15% of the first. Therefore, Eq. (A.15) should generally be a good approximation for the first term of Eq. (A.1) in low-frequency cryocooler regenerators with small r_h/δ_κ. It may be prudent to account for the second term of Eq. (A.14) if utmost accuracy is desired, especially at temperatures not near T_c or T_w.

A.3. Simplifying the $|U_1|^2$ power term

The same Taylor series expansion for f_j is now used to simplify the $|U_1|^2$ term of Eq. (A.1). The quantity of interest is C_{uu}:

$$C_{uu} = \frac{1}{(1-\sigma)}\frac{1}{|1-f_\nu|^2}\mathrm{Im}\left[\tilde{f}_\nu + \frac{(f_\kappa - \tilde{f}_\nu)(1+\epsilon_s f_\nu/f_\kappa)}{(1+\epsilon_s)(1+\sigma)}\right]. \quad (A.16)$$

Dropping terms of form ${r_h}^p{\delta_\kappa}^q{\delta_\nu}^r$ with $p > 2$, complex algebra gives

$$C_{uu} \approx -\frac{-4{\epsilon_i}^2{r_h}^2 + 105\epsilon_i{\delta_\kappa}^2 + 4{\epsilon_r}^2{r_h}^2 + 106\epsilon_r{r_h}^2 + 102{r_h}^2}{105{\delta_\kappa}^2\left({\epsilon_i}^2 + {\epsilon_r}^2 + 2\epsilon_r + 1\right)}. \quad (A.17)$$

Eliminating terms of order ${\epsilon_i}^2$, the approximate solution is

$$C_{uu} \approx -\left[\frac{\epsilon_i}{(1+\epsilon_r)^2} + \frac{{r_h}^2/{\delta_\kappa}^2}{1+\epsilon_r}\right]. \quad (A.18)$$

Fig. A.1c shows that the error in the approximation for C_{uu} is 4% or less for r_h less than 30 μm. For an even tighter approximation, the second term of Eq. (A.18) can be multiplied by $(4\epsilon_r/105 + 34/35)$, making

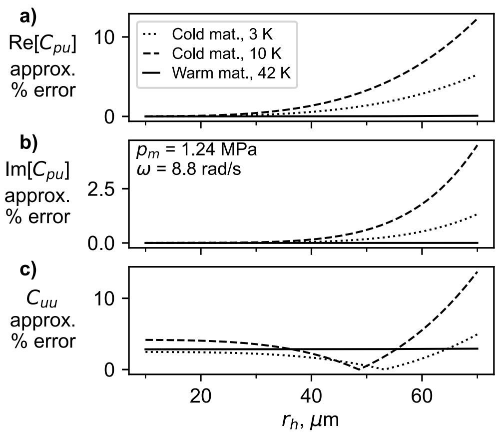

Fig. A.1. The error in the approximations for the real a) and imaginary b) components of C_{pu}. Line styles show the error of the approximations for different temperatures and regenerator materials that are commonly used at the cold or warm ends. The error in the approximation for C_{uu} is shown in c).

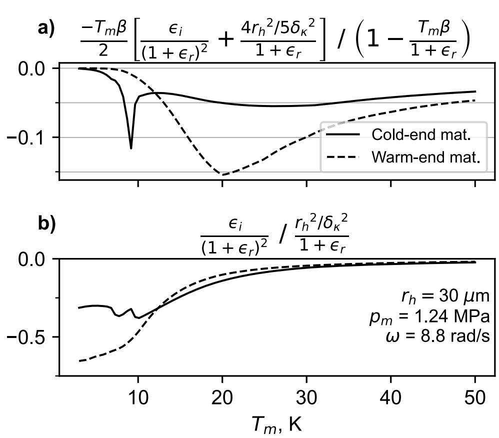

Fig. A.2. a) The coefficient of the second term in Eq. (A.14) normalized by the coefficient of the first term, calculated using solid heat capacities for materials that are commonly used at the warm and cold ends of 4 K regenerators. b) The first term of Eq. (A.18) normalized by the second. Line styles and parameters are the same for both subfigures.

the error less than 1% for r_h less than 30 μm. As shown by Fig. A.2b, the first term of Eq. (A.18) is negligible at the warm end, making the expression for C_{uu} very simple; however, near 4 K, both terms are significant. Inserting C_{uu} back into the total power equation, the simplified form of the $|U_1|^2$ term is:

$$\begin{cases} -\dfrac{\rho_m c_p |U_1|^2}{2\omega A_g (1+\epsilon_r)} \left(\dfrac{r_h}{\delta_\kappa}\right)^2 \dfrac{dT_m}{dx} & \text{for } T_m \approx T_w, \\ -\dfrac{\rho_m c_p |U_1|^2}{2\omega A_g} \left[\dfrac{\epsilon_i}{(1+\epsilon_r)^2} + \dfrac{r_h{}^2/\delta_\kappa{}^2}{(1+\epsilon_r)}\right] \dfrac{dT_m}{dx} & \text{for } T_c \le T_m \le T_w. \end{cases} \tag{A.19}$$

As discussed in Section 4.2, we also write the $|U_1|^2$ power term as $f_2 dT_m/dx$. We have numerically evaluated f_2 using the simplified and full[20] forms of Eq. (A.19) for temperatures near T_c and T_w by estimating U_1 as mostly real, so $|U_1|^2 \approx (2\dot{E}_2/p_1)^2$, where $\dot{E}_2$ was calculated according to the discussion in Appendix C. This result is plotted in Fig. A.3.

[20] The full form includes the ϵ_i term; however, our estimate for ϵ_i contains a fair amount of uncertainty because we were unable to find complete measurements for the thermal conductivity of low-temperature regenerator materials.

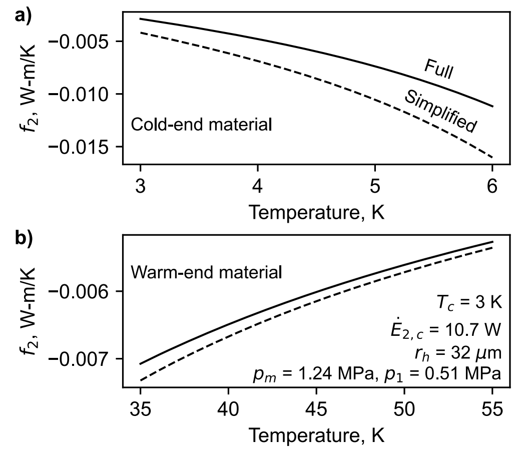

Fig. A.3. Calculation of f_2 at the cold end a) and the warm end b) using pressure and acoustic power estimates from the cryocooler studied here. Material properties come from regenerator materials that are commonly used at the cold and warm ends of 4 K PTRs. Solid lines were calculated using the full form of Eq. (A.19) while the dashed lines were calculated using the simplified form (valid when $|\epsilon_i| << r_h{}^2/\delta_\kappa{}^2$).

Appendix B. Estimates for acoustic power, total power, and streaming when $T_c \neq T_{min}$

B.1. Power estimates

A methodology for estimating acoustic power at the cold end of the regenerator $\dot{E}_{2,c}$ has previously been developed [9]. The First Law was applied to the cold heat exchanger, assuming that power through the buffer tube is equal to $\dot{E}_{2,c} + \dot{N}mh_c$ and that power into the heat exchanger is equal to $\dot{H}_{\beta,c} + \dot{H}_{\epsilon,c} + \dot{N}mh_c + \dot{Q}_c$, so $\dot{Q}_c = \dot{E}_{2,c} - \dot{H}_{\beta,c} - \dot{H}_{\epsilon,c}$. In [9] no power terms proportional to the temperature gradient affect the calculation for $\dot{Q}_c$: a result of our assumption that $dT_m/dx \approx 0$ at the cold end of the second stage regenerator and thermal buffer tube.

As seen in Fig. 11b, end effects may cause the minimum temperature T_{min} to be at $x/L < 1$. Then the analysis of [9] is invalid, as $\dot{H}_2$ is determined by the location in the regenerator near the cold end where $dT_m/dx = 0$:

$$\dot{H}_2 \approx \left(1 - \frac{(T_m\beta)_{min}}{1+\epsilon_{r,min}}\right) \dot{E}_{2,min} + \dot{N}mh_{min}, \tag{B.1}$$

where subscript min denotes evaluation at the minimum temperature. The acoustic power at the minimum temperature of the regenerator is related to that at the cold end by

$$\dot{E}_{2,min} = \dot{E}_{2,c} \exp\left(\int_{T_c}^{T_{min}} \frac{\beta}{1+\epsilon_r}\, dT_m\right) \tag{B.2}$$

as discussed in Appendix C. The appropriate material for calculating ϵ_r is that at the regenerator's coldest section.

The First Law at the cold heat exchanger then gives

$$\dot{E}_{2,c} \approx \dot{Q}_c \left[1 - \exp\left(\int_{T_c}^{T_{min}} \frac{\beta}{1+\epsilon_r}\, dT_m\right) \left(1 - \frac{(T_m\beta)_{min}}{1+\epsilon_{r,min}}\right)\right]^{-1}, \tag{B.3}$$

assuming that $\dot{N}m(h_c - h_{min})$ is negligible. In the above, $\dot{Q}_c$ is the gross cooling power, which is the measured cooling power plus any losses: $\dot{Q}_c = \dot{Q}_{measured} + \dot{Q}_{loss}$. Possible sources of loss include thermal radiation through the buffer tube from the room-temperature flange, and hydraulic minor losses at the transition between heat exchanger and buffer tube. In practice, we measure cooling power over a range of T_c (a few kelvins) and use a linear regression of $\dot{Q}_{measured}$ vs the bracketed term of Eq. (B.3) to estimate fixed parameters $\dot{E}_{2,c}$ and $\dot{Q}_{loss}$ as the

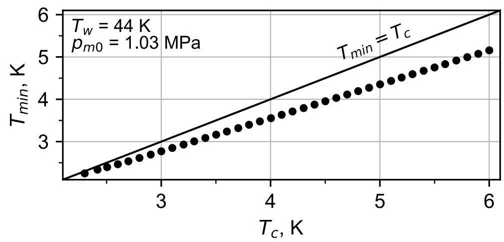

Fig. B.1. The minimum temperature measured near the regenerator cold end vs the temperature measured on the cold heat exchanger. No heat was applied to the regenerator.

slope and intercept, respectively. Such a linear regression fits the data well (coefficient of determination $r^2 > 0.999$), and gives $\dot{E}_{2,c}$ equal to 10.7 W (with T_w = 42 K and p_{m0} = 1.24 MPa) and a fixed loss of 0.11 W.

In the cryocooler studied here, the minimum temperature of the regenerator is observed to be about 2.75 K when T_c is regulated to 3 K, as shown in Fig. B.1. This discrepancy grows linearly as T_c is raised and more heat is required to regulate the cold heat exchanger. Even the relatively small difference between T_c and T_{min} near 3 K or 4 K is significant for calculating $\dot{E}_{2,c}$, as small changes to temperature result in relatively large changes to power. For example, if $\dot{E}_{2,c}$ from Eq. (B.3) is estimated again but using $T_{min} = T_c$, the result drops from 10.7 W to 8.4 W.

B.2. Streaming estimate

At the warm end dT_m/dx may be driven to zero by injecting a large amount of intermediate heat near the center of the regenerator (this cryocooler requires a few watts). Power at both ends can then be calculated using only the relatively simple equations for $\dot{H}_\beta$, $\dot{H}_\epsilon$, and $\dot{H}_m$ (Eq. (2)). While details can be found in [9], $\dot{N}$ easily follows from the First Law using $\dot{H}_{2,w} = \dot{H}_{2,c} - \dot{Q}_{int}$.

The $\dot{N}$ estimate given in [9] should be slightly more accurate if power components are found using T_{min} instead of T_c. Additionally, in that source, $\dot{H}_\beta$ was ignored at the warm end because $T_m\beta$ is very close to 1 at temperatures greater than about 30 K. However, $\dot{H}_\beta$ should still be accounted for because acoustic power is relatively large at the warm end. With these two improvements to the estimate, $\dot{N}$ is given as

$$\dot{N} \approx \frac{\left(1 - \frac{(T_m\beta)_{min}}{1+\epsilon_{r,min}}\right)\dot{E}_{2,min} - \left(1 - \frac{(T_m\beta)_{flat}}{1+\epsilon_{r,flat}}\right)\dot{E}_{2,flat} - \dot{Q}_{int}}{m(h_{flat} - h_{min})}, \tag{B.4}$$

where subscript $flat$ denotes evaluation at the temperature near the warm end where $dT_m/dx = 0$. For the cryocooler studied here, T_{flat} is a few kelvin higher than T_w (Fig. 11b).

The acoustic power at T_{flat} is calculated as discussed in Appendix C. When $dT_m/dx \approx 0$ at both the cold and warm ends, it is approximately true that the entire temperature span is occupied by the middle of the regenerator, so it should be relatively accurate to calculate ϵ_r for use in Eq. (C.5) using only the heat capacity and density of the middle material (i.e., without knowledge of the transition temperatures between materials). However, since we measured the entire temperature profile during these experiments, we calculated ϵ_r in Eq. (C.5) using the appropriate transition temperature between the middle regenerator material and the material at the cold end.

Appendix C. Acoustic power scaling through the regenerator

Two of the significant power terms in low temperature regenerators ($\dot{H}_\beta$ and $\dot{H}_\epsilon$) are proportional to acoustic power $\dot{E}_2$. To understand which power terms are most significant at an arbitrary position within the regenerator, it is critical to understand the evolution of $\dot{E}_2$ at all

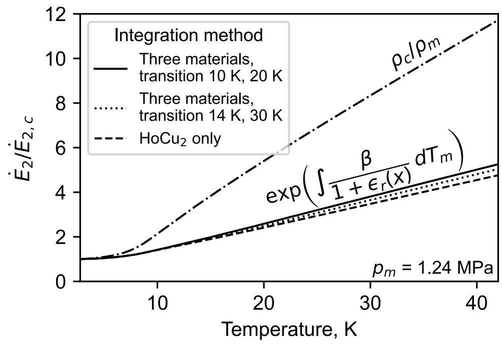

Fig. C.1. Scaling of acoustic power at temperatures between 2.75 K and 42 K, normalized by acoustic power at 2.75 K. The line labeled ρ_c/ρ_m gives the scaling in a regenerator with infinite heat capacity, while the other lines account for finite heat capacity assuming different regenerator materials and transition temperatures between those materials (please see text for details).

temperatures between T_c and T_w. In Appendix B we discussed how $\dot{E}_2$ at T_c ($\dot{E}_{2,c}$) is estimated; here we will discuss how to calculate $\dot{E}_2$ at other temperatures.

Acoustic power changes according to

$$\frac{d\dot{E}_2}{dx} = \frac{1}{2}\mathrm{Re}\left[\widetilde{U_1}\frac{dp_1}{dx} + \tilde{p_1}\frac{dU_1}{dx}\right]. \tag{C.1}$$

Following the approach in [15] the above is written as

$$\frac{d\dot{E}_2}{dx} = -\frac{r_\nu}{2}|U_1|^2 - \frac{1}{2r_\kappa}|p_1|^2 + \frac{1}{2}\mathrm{Re}[g\tilde{p}_1 U_1]. \tag{C.2}$$

In non-tortuous regenerators (such as those made with parallel plates) and with real-fluid properties and nonzero ϵ_s,

$$g = \frac{\beta(f_\kappa - f_\nu)}{(1-f_\nu)(1-\sigma)(1+\epsilon_s)}\frac{dT_m}{dx}. \tag{C.3}$$

The first two terms of Eq. (C.2) are viscous dissipation and thermal relaxation dissipation, respectively. For the low frequency, small r_h/δ_κ cryocoolers of interest in this manuscript, these two terms are small and therefore neglected.

The third term of Eq. (C.2) represents either a source or sink of acoustic power and is critical in thermoacoustic components with nonzero temperature gradient. In the regenerators of engines (where dT_m/dx and $\dot{E}_2$ have the same sign) the term amplifies acoustic power and in the regenerators of refrigerators (where dT_m/dx and $\dot{E}_2$ have opposite signs) it attenuates acoustic power. For regenerators with $r_h << \delta_\kappa$ and δ_ν, $(f_\kappa - f_\nu)/(1-f_\nu)(1-\sigma) \approx 1$, so g in Eq. (C.2) can be estimated as real and Eq. (C.2) may be rewritten as

$$\frac{1}{\dot{E}_2}\frac{d\dot{E}_2}{dx} \approx g \approx \frac{\beta}{1+\epsilon_r(x)}\frac{dT_m}{dx}, \tag{C.4}$$

assuming that the real part of ϵ_s is much larger than the imaginary part. Here ϵ_r is written $\epsilon_r(x)$ to emphasize that this quantity is not only temperature dependent, but also position dependent in regenerators made with multiple materials (as is common in 4 K cryocoolers).

Acoustic power at any temperature in the regenerator can then be found by integrating Eq. (C.4) between T_c and the temperature of interest. For example, acoustic power at the warm end is

$$\dot{E}_{2,w} \approx \dot{E}_{2,c}\exp\left(\int_{T_c}^{T_w} \frac{\beta}{1+\epsilon_r(x)}\, dT_m\right). \tag{C.5}$$

Note that for a regenerator with infinite solid heat capacity, the integral in Eq. (C.5) becomes $\int \beta\, dT_m = -\int \rho^{-1} d\rho$, and acoustic power at the warm end is simply $\dot{E}_{2,c}\rho_c/\rho_w$. This result is plotted in Fig. C.1.

For a regenerator made of a single material, integration of Eq. (C.5) is straightforward; however, for a regenerator made of multiple materials, the most accurate evaluation of Eq. (C.5) requires knowledge of the temperature spanned by each regenerator material. In this manuscript, acoustic power at temperatures other than T_c was calculated[21] by assuming that the transitions between the three materials were at 10 K and 20 K. This only gives an estimate of the acoustic power at temperatures not equal to T_c because those are only estimates of the transition temperatures, and the temperature of the regenerator at the material transitions changes as heat is applied to the regenerator. However, we also integrated Eq. (C.5) with transition temperatures equal to 14 K and 30 K. The resulting $\dot{E}_{2,w}$ differed by only 4% between the two cases, suggesting that precise tracking of the transition temperature is unnecessary for satisfactory accuracy.

Equation (C.5) was also calculated by assuming that the entire regenerator was built from $HoCu_2$, resulting in $\dot{E}_{2,w}$ only about 9% different from the more robust integration using three materials. This shows that a reasonable estimate for the acoustic power throughout the regenerator may be obtained without knowledge of the temperature profile. Holmium copper was selected as the material for this integration because it has significant heat capacity at temperatures near and above 4 K, which is in contrast to another commonly used cold-end material (GOS) which has relatively low heat capacity at temperatures above about 6 K.

The results are plotted in Fig. C.1. At 42 K, the appropriate $\dot{E}_2$ (calculated using Eq. (C.5)) is less than half of that calculated assuming infinite solid heat capacity (using ρ_c/ρ_m). Much of the discrepancy between these two calculations seems to develop at temperatures around 9 K, where helium at p_m near 1.2 MPa has a large spike in heat capacity and ϵ_r is large.

The accuracy of Eq. (C.5) was checked against the numerical models generated in REGEN3.3 and DeltaEC for the analysis given in Supplementary 1. The warm-end acoustic power calculated by Eq. (C.5) was within about 2% of that output by DeltaEC; good agreement was expected because the DeltaEC model used a parallel plate geometry and did not account for Reynolds number dependence of friction factors or heat-transfer coefficients, just as the derivation of Eq. (C.5) did not account for Reynolds number dependence. Agreement with REGEN3.3 was worse but still reasonable: $\dot{E}_{2,w}$ calculated by Eq. (C.5) had an error of about 10%.

Appendix D. Supplementary material

Supplementary material related to this article can be found online at https://doi.org/10.1016/j.cryogenics.2023.103685.

References

[1] Uhlig K. 3He/4He dilution refrigerator with high cooling capacity and direct pulse tube pre-cooling. Cryogenics 2008;48(11):511–4. https://doi.org/10.1016/j.cryogenics.2008.07.004.

[2] Radebaugh R, Marquardt ED, Gary J, O'Gallagher A. Regenerator behavior with heat input or removal at intermediate temperatures. In: Ross RG, editor. Cryocoolers 11. Boston, MA: Springer US; 2002. p. 409–18.

[3] Zhu S, Ichikawa M, Nogawa M, Inoue T. 4 K pulse tube refrigerator and excess cooling power. AIP Conf Proc 2002;613(1):633–40. https://doi.org/10.1063/1.1472075.

[4] Ravex A, Trollier T, Tanchon J, Prouvé T. Free third-stage cooling for two-stage 4 K pulse tube cryocooler. In: Cryocoolers 14; 2007. p. 157–61.

[5] Prouvé T, Godfrin H, Gianèse C, Triqueneaux S, Ravex A. Experimental results on the free cooling power available on 4K pulse tube coolers. J Phys Conf Ser 2009;150(1):012038. https://doi.org/10.1088/1742-6596/150/1/012038.

[6] Wang C. Extracting cooling from the pulse tube and regenerator in a 4 K pulse tube cryocooler. In: Cryocoolers 15; 2009. p. 177–84.

[7] de Waele ATAM, Xu MY, Ju YL. Nonideal-gas effect in regenerators. Cryogenics 1999;39(10):847–51. https://doi.org/10.1016/S0011-2275(99)00102-2.

[8] Cao Q, Qiu L, Gan Z. Real gas effects on the temperature profile of regenerators. Cryogenics 2014;61:31–7. https://doi.org/10.1016/j.cryogenics.2014.01.011.

[9] Snodgrass R, Kotsubo V, Ullom J, Backhaus S. Leveraging real fluid effects as a tool for power flow measurements in 4 K cryocooler regenerators. Cryocoolers 2021;21:315–24.

[10] Snodgrass R, Ullom J. Direct cooling from the regenerators of Gifford-McMahon cryocoolers, with comparison to pulse tube refrigerators. Cryogenics 2022;124:103473. https://doi.org/10.1016/j.cryogenics.2022.103473.

[11] Snodgrass R, Ullom J, Backhaus S. Optimal absorption of distributed and conductive heat loads with cryocooler regenerators. IOP Conf Ser, Mater Sci Eng 2022;1240(1):012131. https://doi.org/10.1088/1757-899X/1240/1/012131.

[12] Snodgrass R, Kotsubo V, Ullom J, Backhaus S. A temperature instability in 4 K cryocooler regenerators caused by real fluid properties. Cryocoolers 2021;21:305–13.

[13] Tan H, Tan J, Zhao B, Zhao Y, Xue R, Wu S, et al. Investigations on a 2.2 K five-stage Stirling-type pulse tube cryocooler. Part A: Theoretical analyses and modeling. Cryogenics 2023;129:103630. https://doi.org/10.1016/j.cryogenics.2023.103630.

[14] Rott N. Thermoacoustics. Advances in applied mechanics, vol. 20. Elsevier; 1980. p. 135–75.

[15] Swift GW. Thermoacoustics: a unifying perspective for some engines and refrigerators. 2nd edition. Springer International Publishing; 2017.

[16] Wang C, Gifford PE. Development of 4 K pulse tube cryorefrigerators at Cryomech. AIP Conf Proc 2002;613(1):641–8. https://doi.org/10.1063/1.1472076.

[17] Snodgrass R, Ullom J, Backhaus S. Role of non-temperature-gradient power flow terms in low-temperature regenerators. Cryocoolers 2022;22:291–302.

[18] Shaowei Z, Peiyi W, Zhongqi C. Double inlet pulse tube refrigerators: an important improvement. Cryogenics 1990;30(6):514–20. https://doi.org/10.1016/0011-2275(90)90051-D.

[19] Gedeon D. DC gas flows in Stirling and pulse tube cryocoolers. In: Ross RG, editor. Cryocoolers 9. Boston, MA: Springer US; 1997. p. 385–92.

[20] Lang A, Häfner H-U, Heiden C. Systematic investigations of regenerators for 4.2K-refrigerators. In: Kittel P, editor. Advances in cryogenic engineering, advances in cryogenic engineering. Boston, MA: Springer US; 1998. p. 1573–80.

[21] Wang C. Numerical analysis of 4 K pulse tube coolers: Part I. Numerical simulation. Cryogenics 1997;37(4):207–13. https://doi.org/10.1016/S0011-2275(97)00013-1.

[22] Zhao DZ, Wang DC. Cryogenic engineering and technologies: principles and applications of cryogen-free systems. CRC Press; 2019.

[23] Wang C, Thummes G, Heiden C. Effects of DC gas flow on performance of two-stage 4K pulse tube coolers. Cryogenics 1998;38(6):689–95. https://doi.org/10.1016/S0011-2275(98)00044-7.

[24] Wang C, Thummes G, Heiden C. Control of DC gas flow in a single-stage double-inlet pulse tube cooler. Cryogenics 1998;38(8):843–7. https://doi.org/10.1016/S0011-2275(98)00070-8.

[25] Bell IH, Wronski J, Quoilin S, Lemort V. Pure and pseudo-pure fluid thermophysical property evaluation and the open-source thermophysical property library CoolProp. Ind Eng Chem Res 2014;53(6):2498–508. https://doi.org/10.1021/ie4033999.

[26] Swift GW. Thermoacoustic engines. J Acoust Soc Am 1988;84(4):1145–80. https://doi.org/10.1121/1.396617.

[27] Ward B, Clark J, Swift G. Users guide for DeltaEC: design environment for low-amplitude thermoacoustic energy conversion. www.lanl.gov/thermoacoustics, 2017.

[28] Meurer A, Smith CP, Paprocki M, Čertík O, Kirpichev SB, Rocklin M, et al. SymPy: symbolic computing in Python. PeerJ Comput Sci 2017;3:e103. https://doi.org/10.7717/peerj-cs.103.

[21] Except for the results of Fig. 12a. In that plot, $\dot{E}_2(T_m)$ was calculated using the appropriate ϵ_r for each material.